Published in final edited form as:

Immunity. 2023 December 12; 56(12): 2699–2718.e11. doi:10.1016/j.immuni.2023.11.005.

Stat5 opposes the transcription factor Tox and rewires exhausted CD8+ T cells towards durable effector-like states during chronic antigen exposure

Jean-Christophe Beltra[1,2,3], **Mohamed S. Abdel-Hakeem**[1,2,4,5], **Sasikanth Manne**[1,2], **Zhen Zhang**[6], **Hua Huang**[6], **Makoto Kurachi**[7], **Leon Su**[8], **Lora Picton**[8], **Shin Foong Ngiow**[1,2], **Yuki Muroyama**[1,2], **Valentina Casella**[9], **Yinghui J. Huang**[1,2], **Josephine R. Giles**[1,2,3], **Divij Mathew**[1,2], **Jonathan Belman**[1,2], **Max Klapholz**[1,2], **Hélène Decaluwe**[10], **Alexander C. Huang**[2,3,11,12], **Shelley L. Berger**[6], **K. Christopher Garcia**[8,13,14,15], **E. John Wherry**[1,2,3,16]

[1]Department of Systems Pharmacology and Translational Therapeutics, University of Pennsylvania, PA, USA

[2]Institute for Immunology and Immune Health, Perelman School of Medicine, University of Pennsylvania, Philadelphia, PA, USA

[3]Parker Institute for Cancer Immunotherapy at University of Pennsylvania, Philadelphia, PA, USA

[4]Department of Microbiology and Immunology, Faculty of Pharmacy, Cairo University, Kasr El-Aini, Cairo 11562, Egypt

[5]Current address: Department of Pathology and Laboratory Medicine, Emory University School of Medicine, Atlanta, GA, USA

[6]Department of Cell and Developmental Biology, Penn Epigenetics Institute, Perelman School of Medicine, Philadelphia, PA 19104, USA

[7]Department of Molecular Genetics, Graduate School of Medical Sciences, Kanazawa University, Kanazawa 920-8640, Japan

[8]Departments of Molecular and Cellular Physiology and Structural Biology, Stanford University School of Medicine, Stanford, CA 94305, USA

[9]Infection Biology Laboratory, Department of Medicine and Life Sciences, Universitat Pompeu Fabra, Barcelona, Spains

[*]Correspondence: wherry@pennmedicine.upenn.edu.

Author Contributions

J.C-B and E.J.W conceived and designed the experiments. J.C-B performed the experiments with help from M.S.A-H, Y.M, V.C, S.F.N, D.M, J.B and M.K. J.C-B prepared libraries and performed sequencing with help from D.M and A.C.H. J.C-B analyzed the scRNAseq and CITEseq datasets with help and guidance from S.M. ATACseq datasets were analyzed by S.M and H.H in collaboration with J.C-B. Z.Z and S.L-B provided technical help for CnR and CnR datasets were analyzed by H.H in collaboration with J.C-B. L.S, L.P and K-C.G provided the orthogonal IL2Rβ construct. M.K adapted the STAT5CA construct to our MSCV based expression system. J.C-B and E.J.W wrote the manuscript with input from J.R.G, H.D and A.C.H.

[10]Cytokines and Adaptive Immunity Laboratory, Sainte-Justine University Hospital Research Center, Montreal, Quebec, Canada; Department of Microbiology and Immunology, Faculty of Medicine, University of Montreal, Montreal, Quebec, Canada; Immunology and Rheumatology Division, Department of Pediatrics, Faculty of Medicine, University of Montreal, Montreal, Quebec, Canada

[11]Department of Medicine, Perelman School of Medicine, University of Pennsylvania, Philadelphia, Pennsylvania 19104, USA

[12]Abramson Cancer Center, Perelman School of Medicine, University of Pennsylvania, PA, USA

[13]Stanford Cancer Institute, Stanford University School of Medicine, Stanford, CA 94305, USA.

[14]Parker Institute for Cancer Immunotherapy, 1 Letterman Drive, Suite D3500, San Francisco, CA 94129, USA.

[15]Howard Hughes Medical Institute, Stanford University School of Medicine, Stanford, CA 94305, USA

[16]Lead contact

Summary

Rewiring exhausted $CD8^+$ T (Tex) cells towards functional states remains a therapeutic challenge. Tex cells are epigenetically programmed by the transcription factor Tox. However, epigenetic remodeling occurs as Tex cells transition from progenitor (Tex^{prog}), to intermediate (Tex^{int}) and terminal (Tex^{term}) subsets suggesting development flexibility. We examined epigenetic transitions between Tex cell subsets and revealed a reciprocally antagonistic circuit between Stat5a and Tox. Stat5 directed Tex^{int} cell formation and re-instigated partial effector-biology during this Tex^{prog} to Tex^{int} cell transition. Constitutive Stat5a activity antagonized Tox and rewired $CD8^+$ T cells from exhaustion to a durable effector and/or NK-like state with superior anti-tumor potential. Temporal induction of Stat5-activity in Tex cells using an orthogonal IL-2:IL2Rβ-pair fostered Tex^{int} cell accumulation, particularly upon PD-L1 blockade. Re-engaging Stat5 also partially reprogrammed the epigenetic landscape of exhaustion and restored polyfunctionality. These data highlight therapeutic opportunities of manipulating the IL-2-Stat5 axis to rewire Tex cells towards more durably protective states.

Graphical Abstract

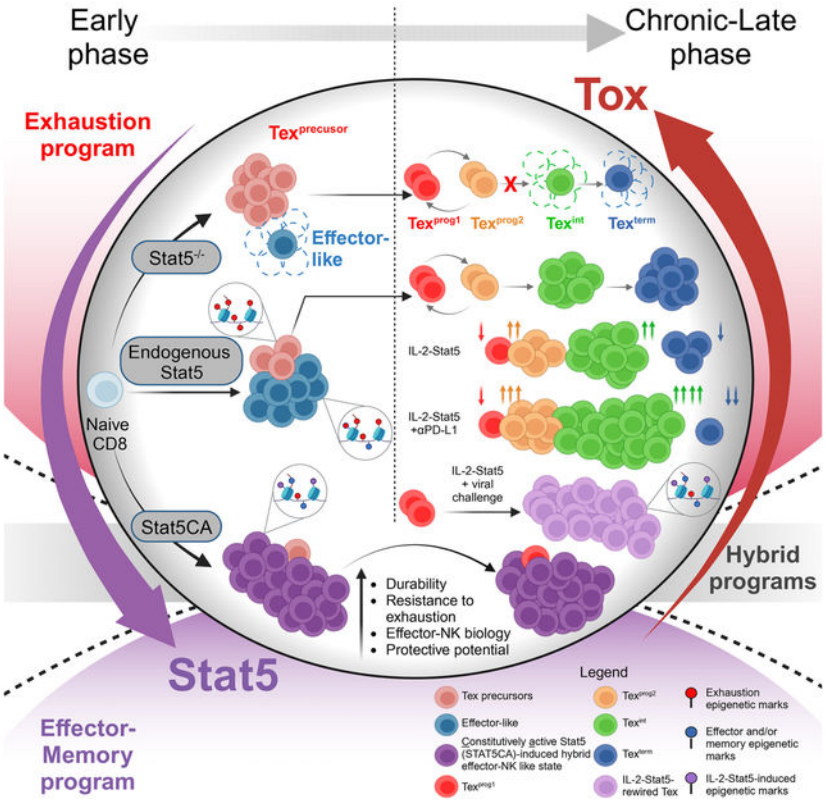

eToc

Reversing CD8$^+$ T cell exhaustion is a major challenge of cancer immunotherapy. Yet, the epigenetic stability of the exhaustion program remains a key hinderance. Beltra et *al.* identify the transcription factor Stat5 as a key axis to exploit for rewiring exhausted CD8$^+$ T cells towards more durably protective states.

Keywords

CD8$^+$ T cell exhaustion; Stat5; IL-2; epigenetic reprogramming; Tox; PD-1 blockade; Tex intermediate; orthogonal IL-2:IL2Rβ

INTRODUCTION

CD8$^+$ T cell exhaustion limits effective control of chronic viral infections and tumors and is a major barrier to anti-cancer immunotherapies.[1,2,3] First described as loss of functions in settings of chronic antigenic stimulation,[4,5] it is now clear that CD8$^+$ T cell exhaustion represents a distinct epigenetically programmed state of T cell differentiation initiated by the HMG-transcription factor (TF) Tox.[6–10] This Tox-dependent program allows exhausted CD8$^+$ T (Tex) cells to persist during chronic viral infection and cancer but precludes further developmental plasticity towards functional effector (Teff) or memory (Tmem) CD8$^+$ T cells.[2,11–15] Relieving some inhibition of Tex cells through PD-1 pathway blockade results in considerable clinical efficacy for some cancers.[16–21] Nevertheless, PD-1 pathway

blockade fails to result in epigenetic rewiring of Tex cells[22,23] highlighting the need for complementary strategies to relieve the (de)differentiation constraints of Tex cells and achieve more protective states.

Tex cells form a distinct branch of mature $CD8^+$ T cell differentiation with major epigenetic divergence from Teff and Tmem cells generated upon acutely resolving infections or vaccinations.[24–27] Moreover, the Tex "lineage" exists as a developmental hierarchy. For example, a Tcf1 (*Tcf7*)-expressing progenitor (Tex^{prog}) subset retains proliferative potential and continuously repopulates downstream Tex cell subsets.[24,28–30] These Tex^{prog} exist in two interchangeable states including a stem-like - quiescent subset (Tex^{prog1}) that resides in lymphoid tissues and a transcriptionally distinct subpopulation (Tex^{prog2}) that leaves these lymphoid niches and re-enters cell-cycle. As these Tex^{prog2} cells proliferate, they lose Tcf1 expression and differentiate into an intermediate "effector-like" subset (Tex^{int}) that circulates in blood and ultimately converts to terminally exhausted $CD8^+$ T cells (Tex^{term}) upon entering peripheral tissues where these Tex^{term} cells also acquire features of tissue residency.[24] This Tex^{term} subset can arise directly from Tex^{int} cells[24,25] or possibly directly transitioning from the Tex^{prog} subsets.[26] Other Tex cell subpopulations have also recently been described including Tex^{ISG}, Tex^{KLR} and Tex^{STR} cells that also likely represent intermediate states in this Tex differentiation hierarchy.[23,31–33] The biology of these Tex subsets has therapeutic relevance. For example, whereas Tex^{prog} cells are the targets of PD-1 blockade and initiate the proliferative response,[28,29] this therapy culminates in a transient amplification of "effector-like" Tex^{int} cells, a key biological event for therapeutic benefit.[24,25] This Tex^{int} population re-acquires some effector features, though remains unable to fully engage effector biology or sustain durable benefit due to a largely inflexible Tox-dependent epigenetic landscape.[24–26] Whether the conversion between Tex subsets in this developmental hierarchy provides opportunities to drive more substantial epigenetic rewiring and therapeutic potential remains an open question.

Here, we discovered a reciprocal antagonistic circuit between Tox and Stat5a in Tex cells including preferential re-engagement of Stat5a activity in the T_{EX}^{int} subset. Stat5 fostered Tex^{int} cell development, re-engaged effector circuitry in this subset and enabled Tex cell responses to PD-L1 blockade. Enforcing constitutive Stat5a activity (STAT5CA) antagonized Tox, provoking epigenetic and transcriptional rewiring of $CD8^+$ T cells towards a durable "effector-like" state expressing NK receptors and displaying superior anti-tumor activity. Enforcing Stat5 activity in established Tex cells using an orthogonal IL-2:IL2Rβ pair system[34] boosted Tex^{int} cell formation, particularly in combination with PD-L1 blockade. Finally, temporal reactivation of Stat5 in Tex^{prog} cells reversed key epigenetic features of exhaustion allowing *de novo* accessibility at Teff-Tmem cell-related open chromatin regions and restored polyfunctionality. Together, we identify Stat5 as a key regulator of Tex cell differentiation, antagonizing Tox-driven terminal exhaustion and fostering improved effector activity and durability in the setting of chronic antigen (Ag) stimulation. Moreover, therapeutically augmenting IL-2:Stat5 signals specifically in Tex cells in combination with PD-1 pathway blockade not only expanded the Tex^{int} population but also rewired these Tex cells towards a more protective differentiation state with features of durability under chronic antigenic stress and enhanced effector biology.

Results

Tox restrains Stat5a activity in virus-specific CD8$^+$ T cells during chronic infection

During chronic viral infections and cancer, Tox directs Ag-specific CD8$^+$ T cells towards exhaustion and antagonizes development of functional Teff and Tmem cells.[6–9] However, re-engagement of some effector circuitry occurs as Tex^{prog} cells transition to the Tex^{int} subset, a developmental step also associated with a transient, partial, reduction in Tox expression[24] suggesting the existence of transcriptional circuits antagonizing *Tox*. To identify such transcriptional circuits, we investigated gene networks and upstream transcription factors (TFs) preferentially antagonized by Tox in virus-specific CD8$^+$ T cells. Ingenuity Pathways Analysis (IPA) on differentially expressed genes (DEGs) between lymphocytic choriomeningitis virus (LCMV)-specific WT and Tox-deficient CD8$^+$ T cells (extracted from available RNA sequencing [RNAseq] data),[7] indicated increased activity of regulators of interferon signaling (i.e. *Irf1*, *Irf7*, *Stat1*) and terminal exhaustion (i.e. *Foxo1*) in WT cells (Fig. 1A, B). Conversely, Teff or Tmem-related TFs (i.e. *Tbx21*, *Id3* and *Stat5a*) were more active in Tox-deficient cells (Fig. 1B, Table S1). Using a second single-cell RNAseq (scRNAseq) dataset,[6] transcriptional networks of Tbet and Stat5a strongly enriched in Tox-deficient compared to WT LCMV-specific CD8$^+$ T cells (Fig. S1A–E, Table S1). Among the transcriptional regulators identified by IPA, Tbet and Stat5a overlapped with a list of TFs independently predicted using Taiji analysis[35] to selectively impact Tex^{int} cells compared to other Tex subsets (Fig. 1C).[24] Previous work identified bi-directional antagonism between Tbet and Tox in Tex^{int} cells.[24] However, Taiji analysis predicted Stat5a activity to be even more enriched in the Tex^{int} subset than Tbet, and the IPA-defined transcriptional network of Stat5a was more strongly anti-correlated with Tox expression than Tbet (Fig. 1C, D). These analyses suggested a possible antagonistic axis between Tox and Stat5a in Tex cells. Indeed, the transcriptional signatures of Stat5a and Tox were inversely correlated in Ag-specific CD8$^+$ T cells at 1 week and 1 month of chronic infection (Fig. 1E, F). Stat5a activity in Tex cells was also anti-correlated with the expression of exhaustion-specific genes, but positively associated with genes involved in effector biology (Fig. S1F). These data suggested a role for Stat5a in antagonizing Tox and the program of CD8$^+$ T cell exhaustion.

Stat5a reduces Tox expression and fosters effector-like CD8$^+$ T cell differentiation during chronic viral infection

The potential Stat5a and Tox antagonism observed above was evident by d8p.i. We therefore interrogated the impact of Stat5a early during chronic infection. Congenically distinct LCMV-D^{b}gp$_{33–41}$-specific P14 CD8$^+$ T cells were transduced with retroviruses (RV) encoding either a constitutively active form of Stat5a (P14 STAT5CA)[36,37] or a control RV (P14 Empty). Transduced P14 cells were sort-purified based on RV-encoded reporter protein expression (violet-excited [VEX] or green fluorescent protein [GFP]), mixed (1:1) and co-transferred into congenically distinct LCMV clone 13 (Cl13) infected mice (Fig. 2A). Early during chronic infection at d8 p.i., P14 cells differentiated into either highly activated "effector-like" (Tcf1:Ly108$^-$Tim3$^+$) or precursors of Tex (Tex^{prec}; Tcf1:Ly108$^+$Tim3$^-$) cells (Fig. S2A).[23,30,38] Both populations were detected for P14 Empty controls at d8p.i. In contrast, most P14 STAT5CA cells (91.7±0.98%) had differentiated into Ly108$^-$Tim-3$^+$

CD8$^+$ T cells and formed substantially fewer Ly108$^+$Tim-3$^-$ Tex^{prec} (2.7%±0.4%) compared to P14 Empty controls (25.6%±3.7%) (Fig. 2B and S2B). We further confirmed the decrease in the generation of Tex^{prec} cells in P14 STAT5CA cells using unbiased clustering based on 12 flow cytometry parameters (Fig. 2C-see methods) or Tcf1 expression (Fig. 2D-upper panel). The overall numerical advantage of P14 STAT5CA cells over the P14 Empty (Fig. S2B) suggested a differentiation bias towards the Ly108$^-$Tim-3$^+$ effector-like population at the expense of Tex^{prec} cells. Enforcing Stat5a activity also reduced the per-cell amount of Tox and increased expression of effector-related molecules (Cx3cr1, Granzyme B [GzmB]) (Fig. 2D [lower panel], E). At this time-point, production of antiviral cytokines after gp_{33} peptide stimulation and expression of inhibitory receptors ([IR]; i.e. PD-1, Lag-3, and Tigit) were equivalent between P14 Empty and P14 STAT5CA cells (except for 2B4 and Tim-3 that were more highly expressed by the STAT5CA P14 cells) (Fig. 2E and S2C). Thus, increasing STAT5a activity reduced Tox expression and fostered early development of Ly108$^-$Tim-3$^+$ effector-like cells at the expense of Tex^{prec} cells.

Stat5 supports early expansion of Ag-specific CD8$^+$ T cells in acutely resolving infections, but has minimal impact on the balance of KLRG1$^+$ terminal Teff cells and CD127$^+$ memory precursors in these settings.[39,40] To interrogate how endogenous Stat5 regulates CD8$^+$ T cell differentiation early during chronic viral infection, naïve P14 WT (Rosa^{YFP}*Stat5a-b*$^{+/+}$) and P14 Stat5iKO (Rosa^{YFP}*Stat5a-b*$^{flox/flox}$) were treated with tat-cre recombinase *in vitro* (cre$^+$; or not [cre$^-$]) to induce genetic deletion of *floxed* alleles. These tat-cre treated P14 cells were then adoptively transferred into congenically distinct recipient mice followed by LCMV Cl13 infection (Fig. S2D). Induction of YFP served as a surrogate for efficient cre-mediated recombination. At d8p.i, genetic deletion of *Stat5a-b* increased the proportion of Tex^{prec} cells at the expense of Ly108$^-$Tim-3$^+$ effector-like cells (11±1% vs 47±2% and 85±1% vs 49±2% of Tex^{prec} cells and Ly108$^-$Tim-3$^+$ cells in P14 WT vs P14 Stat5iKO respectively) (Fig. 2F and S2E–F). The number of Stat5iKO P14 cells was reduced by ~11-fold reflecting a loss of Ly108$^-$Tim-3$^+$ cells, whereas the Ly108$^+$Tim-3$^-$ Tex^{prec} cells were less affected (Fig. 2G). Changes in proliferation or cell death as assessed by BrdU incorporation (d7-8) or active caspase-3 did not explain these differences between the WT and *Stat5a-b* iKO cells (Fig. S2G–H). These data suggested an impact of *Stat5a-b* on differentiation of Ly108$^-$Tim-3$^+$ cells, consistent with the enhanced development of this effector-like population using STAT5CA (Fig. 2B). This effect of *Stat5a-b*-deficiency appeared to be preferential to chronic infection because, consistent with previous studies,[39,40] *Stat5a-b* impacted the overall expansion but not the distribution of CD8$^+$ T cell subsets during acute LCMV Armstrong (Arm) infection (Fig. S2I). Consistent with the reduction of Tox upon constitutive activation of Stat5a (Fig. 2D-lower panel), loss of *Stat5a-b* resulted in increased Tox expression in P14 Stat5iKO compared to P14 WT during Cl13 infection (Fig. 2H and S2J). The minimal role of Tox in acute versus chronic infection[6,7] may explain the preferential impact of Stat5 during LCMV Cl13 infection. Together, Stat5 impacted early population dynamics during evolving chronic infection, repressing Tox and fostering differentiation of the effector-like Ly108$^-$Tim-3$^+$ subset.

Constitutive Stat5a activation promotes an epigenetic state with features of effector and exhausted CD8$^+$ T cells during chronic infection

We next investigated whether constitutively active Stat5a altered the early Tox-dependent epigenetic programming of exhaustion. We performed Assay for Transposase-Accessible Chromatin followed by high throughput sequencing (ATACseq)[41] on P14 Empty and P14 STAT5CA cells at d8 of Cl13 infection and also included P14 cells isolated at d8 of Arm infection (Teff). Each population of P14 cells was distinct in principal component space (Fig. 3A) or by Spearman distance analysis (Fig. S3A). P14 Empty and P14 STAT5CA differed from Arm-derived Teff cells by 27,876 and 25,681 differentially accessible peaks (DAPs) respectively (lfc>2, FDR≤0.01) but P14 STAT5CA cells also differed from their P14 Empty counterparts by 16,901 DAPs (Fig. 3B, Table S2). Most DAPs were located at intergenic, promoter and intronic regions (Fig. S3B). The reduced proportion of Ly108$^+$ Tex^{prec} cells in P14 STAT5CA cells at this time-point (Fig. 2B) could contribute to these epigenetic differences. However, only 454 of the 16,901 DAPs (2.7%) between P14 Empty and P14 STAT5CA were associated with genes differentially expressed between WT and *Tcf7*$^{-/-}$ gp33$^+$ CD8$^+$ T cells from d7 post LCMV Cl13 infection (Fig. S3C).[30] Moreover, ATACseq differences were readily apparent even between the Ly108 and Tim-3 subsets of P14 Empty and P14 STAT5CA cells (note, the Ly108$^+$Tim-3$^-$ subset of P14 STAT5CA generated too few cells for analysis; Fig. S3D). Indeed, Ly108$^-$Tim-3$^+$ P14 STAT5CA cells differed from the Ly108$^-$Tim-3$^+$ P14 Empty cells by >1100 DAPs. Moreover, there were more differences between Ly108$^-$Tim-3$^+$ P14 STAT5CA and Ly108$^+$Tim-3$^-$ P14 Empty than between Ly108$^+$Tim-3$^-$ and Ly108$^-$Tim-3$^+$ P14 Empty cells (Fig. S3D–G, Table S2). These data support the notion that STAT5CA was driving epigenetic changes even within individual subsets of developing Tex cells.

To further interrogate the epigenetic impact of constitutive Stat5a expression, we performed K-means clustering of the 16,901 DAPs between P14 Empty and P14 STAT5CA (Fig. 3C, Table S2). Cluster 1 and 4 (C1, 4) captured unique changes for P14 STAT5CA cells. C2, 3 and 5, in contrast contained DAPs that were similarly accessible in P14 STAT5CA and Teff cells but not P14 Empty (Fig. 3C). Overall, among the 16,901 DAPs between P14 Empty and P14 STAT5CA cells, 62% (10,445 peaks; [C2,3 and 5]) represented changes in which P14 STAT5CA cells became more similar to Teff cells compared to P14 Empty cells. DAPs in C1 (gained in P14 STAT5CA) enriched for Stat5 binding motifs (also potentially bound by Stat1, 3 and 4) and motifs for effector-related TFs (Runx1-2) (Fig. 3C–D). C4 DAPs (decreased in P14 STAT5CA) rather contained T-box and homeobox TFs motifs (i.e. Eomes, T-bet, Tbr1, Tbx2-6, Tgif1-2). C2 with high accessibility in P14 Empty included open chromatin regions at exhaustion-related genes (i.e. *Tox*, *Tox2*) and enriched in binding motifs for TCR-dependent TFs with established roles in Tex cell including NFAT (RHD) and BATF (bZIP) (Fig. 3C–D and S3H). C3 and 5 with increased accessibility in both P14 STAT5CA and Teff cells compared to P14 Empty, contained several DAPs located near effector-related genes (i.e. *Gzma*, *Fasl*, *Prf1*, *Runx1-3*, *Id2*) and enriched for Stat5, Runx1-2 and ETS motifs (Fig. 3C–D and S3H). Further clustering of all DAPs between P14 Empty, P14 STAT5CA and Teff cells (70,458 peaks) revealed decreased accessibility at a large fraction of exhaustion-related peaks in P14 STAT5CA cells concomitant with a shift to a more effector-like chromatin landscape (Fig. S3I and Table S2). Together, the altered

epigenetic program in P14 STAT5CA cells was consistent with a shift towards effector biology at a stage when epigenetic imprinting of exhaustion typically occurs.

Consistent with this antagonism of the early program of exhaustion, accessibility at Tox-dependent or exhaustion-related open chromatin regions were reduced in P14 STAT5CA cells, whereas accessibility at effector-associated genomic regions was increased (Fig. 3E and Table S2). In addition, a substantial proportion of Tox, exhaustion or effector signature genes (extracted from indicated datasets) where accessibility varied between P14 STAT5CA and P14 Empty cells possessed one or more Stat5 binding sites (Fig. 3F and Table S2) and, overall, the presence of a Stat5 binding site coincided with greater accessibility changes of overlapping DAPs (Fig. 3G). These observations suggested direct effects on genes involved in effector versus exhaustion biology by Stat5a. *Tox* was among the top exhaustion-related genes with reduced chromatin accessibility in P14 STAT5CA compared to P14 Empty cells and this gene contained one of the highest numbers of direct Stat5 binding sites (Fig. 3H). Analyzing the *Tox* locus revealed remodeling in P14 STAT5CA compared to P14 Empty cells, particularly within the first intron (Fig. 3I). This dense region contained many prominent accessible chromatin regions and active H3K27Ac histone marks in exhausted $CD8^+$ T cells. Moreover, this region included or was framed by several binding sites for NFAT1[42] and NFAT2[43], two key drivers of Tox induction in Tex cells (Fig. 3I, J and S3J, K, Table S2).[6,7,10] Consistent with an active chromatin environment in early Tex cells,[6,7,9,23] the level of chromatin accessibility and active H3K27Ac marks at this dense region in intron 1 correlated with Tox induction (Fig. S3L, M). However, genomic accessibility and accumululation of H3K27Ac marks in this region were noticeably reduced in P14 STAT5CA cells, approaching the accessibility observed in Teff cells (Fig. 3I). The numerous Stat5 binding sites across the *Tox* locus, but especially in intron 1, suggested a direct role for Stat5 in provoking those remodeling (Fig. 3H, I). Together, these data highlight the potential impact of Stat5 in the epigenetic regulation of key exhaustion-related genes including *Tox* where Stat5 appears to function directly to modulate accessibility and transcriptional activity.

Constitutive Stat5a activation promotes a durable effector-NK-like transcriptional state with improved therapeutic potential

Tox drives induction of $CD8^+$ T cell exhaustion, but also is required for the maintenance of Tex cells during chronic infections and cancer.[6–9] Constitutive Stat5a activity antagonized Tox. We, therefore, interrogated the durability and fate of P14 STAT5CA cells later during chronic viral infection. At d27p.i., the P14 STAT5CA cells numerically outcompeted their co-adoptively transferred P14 Empty counterparts in the spleen and peripheral tissues (Fig. 4A–B and S4A–C). This numerical advantage of P14 STAT5CA cells persisted for at least ~3 months in mice with life-long viremia (Cl13 αCD4; Fig. 4A-right and Fig. S4D) indicating a prolonged advantage with enforced STAT5CA expression. This accumulation of P14 STAT5CA cells occurred despite the substantial reduction in $Tcf1^+$ cells (Fig. 2B–D and S2B). To directly test whether this durability could be attributed to $Tcf1^-$ P14 STAT5CA cells, we purified $Ly108^-Tim\text{-}3^+$ ($Tcf1^-$) P14 Empty and P14 STAT5CA cells on d8p.i. and adoptively transferred these cells into infection matched recipients. $Ly108^+Tim\text{-}3^-$ P14 Empty cells were also examined as a control. Although the $Tcf1^+$ P14 Empty cells displayed

the most efficient persistence, Tcf1$^-$ P14 STAT5CA had a robust durability advantage compared to Tcf1$^-$ P14 Empty cells and many more of these STAT5CA cells were recovered 20-days later. (Fig. S4E–F). Therefore, the accumulation advantage of P14 STAT5CA cells reflected, at least in part, better maintenance of the Tcf1$^-$ compartment, though a small population of Tcf1$^+$ P14 STAT5CA cells could also contribute long-term. Thus, constitutive Stat5a activation provides a prolonged accumulation advantage for virus-specific CD8$^+$ T cells during chronic viral infection.

At d27p.i. most P14 STAT5CA cells resembled Ly108$^-$CD69$^-$ Tex^{int} cells. The proportion of Tex^{prog1} (Ly108$^+$CD69$^+$) and Tex^{prog2} (Ly108$^+$CD69$^-$) populations was substantially reduced compared to P14 Empty cells, though a small proportion of the later was present (Fig. 4C and S4G). The frequency of Tex^{term} cells (Ly108$^-$CD69$^+$) was also reduced compared to the P14 Empty (Fig. 4C and S4G). However, the data above from d8p.i. suggested that P14 STAT5CA cells might differ from typical Tex^{int} cells. We, therefore, performed scRNAseq on P14 STAT5CA and P14 Empty cells at ~1-month p.i. We identified canonical clusters of Tex cells including a Tex cell progenitor cluster (C4; progenitors [Tex^{prog}]) selectively expressing *Tcf7, Slamf6,* and *Xcl1* and two clusters with signatures of Tex^{term} cells (C0 and C1), expressing markers of terminal exhaustion (*Cxcr6*)[27] and elevated IRs (*Pdcd1*, *Cd160 and CD244* [2B4]) (Fig. 4D and S4H–I). We also identified two clusters of *Cx3cr1*-expressing cells. One of which was consistent with Tex^{int} cells (C3). The second (C2; Effector-NK-like) also enriched for a Tex^{int} cell signature but displayed selective expression of NK-cell receptors (i.e. *Klre1*, *Klrk1*, *Klrd1*), increased transcripts for effector-related genes (i.e. *Gzma, Zeb2*) and reduced *Tox* and *Pdcd1* compared to all other clusters (Fig. 4D and S4H–I, Table S3). This effector-NK-like cluster (C2) was mainly composed of P14 STAT5CA cells whereas P14 Empty cells rather distributed throughout C0,1,3, and 4 (Fig. 4E and S4J, Table S3). Consistent with the effector-NK-biology in C2, these cells also enriched for the transcriptional signatures of short-lived effector CD8$^+$ T cells (SLEC) and had the lowest enrichment score for an exhaustion or Tox-dependent program (Fig. 4F). Moreover, although the P14 STAT5CA cluster (C2) mapped closely to the Tex^{int} cell cluster (C3) (Fig. 4D), these two clusters differed by expression of 211 genes (Log2FC>0.25, p_value_adj≤0.05) with C3, mostly composed of P14 Empty cells, having higher expression of exhaustion-related genes including *Tox*, *Eomes*, *Pdcd1, Lag3* whereas the P14 STAT5CA cells had higher expression of effector-NK (e.g. *Klre1, Klrb1c, Klrk1, Klrd1*, *Gzma, Tbx21*), and cell survival genes (e.g. *Bcl2* and *Bcl2* interacting proteins) (Fig. 4G–H, S4K and Table S3). Together, constitutive Stat5a activation drove virus-specific CD8$^+$ T cells into a distinct state characterized by effector and NK-like features in a setting that typically drives CD8$^+$ T cell exhaustion.

The accumulation advantage together with this effector-NK biology of P14 STAT5CA cells prompted us to evaluate therapeutic potential. When adoptively transferred into mice with established B16-gp$_{33–41}$ tumors (d10 post tumor inoculation), P14 Empty cells only slightly delayed tumor growth. In contrast, an equal number of P14 STAT5CA cells substantially reduced tumor burden and resulted in survival of all mice to d21 post-tumor inoculation (Fig. 4I–K). Thus, the impact of constitutively active Stat5a on differentiation of CD8$^+$ T cells resulted in improved therapeutic efficacy.

Stat5 is essential for Tex^{int} cell formation and response to PD-L1 blockade

We next used the adoptive transfer approach of P14 WT and P14 Stat5iKO cells (Fig. S2D) to investigate how endogenous Stat5 influenced Tex subset dynamics when exhaustion was fully established. At ~1 month p.i., P14 Stat5iKO cells expressed PD-1 and Tox (albeit slightly less of each compared to P14 WT) but lacked expression of molecules associated with Tex^{int} or Tex^{term} cells (i.e. Granzyme B, Cx3cr1, Tim-3; Fig. 5A). Indeed, the P14 Stat5iKO were almost exclusively composed of Tex progenitor cells (Tex^{prog1} and Tex^{prog2}) with only minor populations of Tex^{int} and Tex^{term} cells compared to P14 WT cells or *Stat5a-b*-proficient (cre^{-}, YFP^{-}) controls from the same donor P14 population (Fig. 5B and Fig. S5A–B). The number of P14 Stat5iKO cells was reduced in the spleen with further reductions in peripheral tissues (typically populated by Tex^{int} and Tex^{term} cells)[24] compared to P14 WT (Fig. 5C and S5C,D). However, the number of Tex^{prog1} and Tex^{prog2} cells was unaffected by *Stat5a-b*-deficiency (Fig. 5C). This stability of Tex^{prog} populations in the absence of *Stat5a-b* contrasted the ~23-fold reduction of Tmem cells generated following an acute LCMV Arm infection in the absence of *Stat5a-b* (Fig. 5D), suggesting distinct requirements for the maintenance of Tmem versus Tex^{prog} cells. PD-L1 blockade did not rescue Tex^{int} cell formation in P14 Stat5iKO and these cells failed to expand following therapy despite a numerically intact progenitor compartment, confirming a defective Tex^{prog2}-to-Tex^{int} cell developmental transition in the absence of *Stat5a-b* (Fig. 5E and S5E,F). In addition, inducible deletion of *Stat5a-b* in mature Tex progenitors compromised *de novo* generation of Tex^{int}-like cells and induction of effector molecules (i.e. Cx3cr1, GzmA, GzmB) in a viral re-challenge assay (Fig. S5G–L). These data implicate Stat5-signals in the formation of the effector-like Tex^{int} subset from Tex^{prog2} cells, a key transition for replenishment of downstream Tex subsets and response to PD-1 pathway blockade.

To investigate the molecular effects of Stat5-deficiency in Tex subsets, we performed Cellular Indexing of Transcriptomes and Epitopes by sequencing (CITEseq) on P14 WT and P14 Stat5iKO cells at ~1 month of chronic infection. RNA-based unsupervised clustering again identified major clusters of Tex cells and confirmed the near absence and robust reduction of the Tex^{int} and Tex^{term} subsets respectively in P14 Stat5iKO compared to P14 WT (Fig. 5F,G and S6A,B, Table S4). Top DEGs between WT and Stat5iKO P14 cells reflected this altered subset distribution with elevated expression of progenitor-associated genes (i.e. *Tcf7*, *Id3*, *Xcl1*) but depletion of genes related to more differentiated subsets (i.e. *Cx3cr1*, *Cxcr6*, *Gzma*, *Gzmb*) in the later population (Fig. 5H, Table S4). Comparing clusters also revealed transcriptional divergence between P14 Stat5iKO and P14 WT cells across all Tex subsets, suggesting that Stat5-deficiency affected all major subsets of Tex cells (Fig. S6C).

The Tex^{prog1} and Tex^{prog2} subsets often co-segregate in scRNAseq space because of the dominance of the progenitor signature. However, the Tex^{prog2} cells engage distinct biology as these cells begin to downregulate *Tcf7*, enter cell cycle and initiate the transition to downstream Tex subsets.[24] CITEseq captured this key transitional biology by discriminating Ly108^{+}CD69^{-} Tex^{prog2} cells using surface markers (including CD69 which is not captured well by scRNAseq) and allowed us to further interrogate Stat5a-b-dependent transcriptional

differences in this subset (Fig. S6D–F). Indeed, analysis of DEGs confirmed transcriptional differences between oligo-tagged antibody-defined Tex subsets (Fig. 5I, Table S4). *Stat5a-b*-deficient Tex^{prog2} cells retained higher expression of progenitor associated-molecules (i.e. *Tcf7*, *Sell*, *Slamf6*, *Id3*, *Tox*) that are otherwise typically reduced during the Tex^{prog1}-to-Tex^{prog2} transition.[24] Some of these progenitor-related molecules even trended higher in the few *Stat5a-b*-deficient Tex^{int} and Tex^{term} cells detectable (e.g. *Sell*, *Slamf6*, *Tcf7*, *Tox*) compared to their P14 WT counterparts (Fig. 5J). In addition, the few Tex^{int} cells detected in P14 Stat5iKO lacked expression of key effector genes (i.e. *Gzma*, *GzmB*, *Cx3cr1*, *Zeb2*, *Tbx21*, *Id2*) and killer lectin-like receptors (KLR; i.e. *Klrd1*, *Klre1*, *Klrc1*, *Klrc2*, *Klrk1*), though because of the small number of Stat5iKO Tex^{int} cells, many of these changes did not reach statistical significance. However, this lack of effector-biology in P14 Stat5iKO Tex^{int} cells was also apparent at the Tex^{term} stage (i.e. reduced *Gzmb*, *Gzma*) and these cells also had reduced expression of *Bcl2* (Fig. 5J). Notably, the Stat5-dependent cyclin *Ccnd2* was reduced in all P14 Stat5iKO subsets compared to their P14 WT counterparts and this change was also coupled to a robust decrease in expression of multiple ribosomal protein-encoding genes (*Rps* genes), particularly in Tex^{prog1} and Tex^{prog2} cells lacking *Stat5a-b* (Fig. 5J). These results suggested an impaired cell-cycle re-entry and sub-optimal *de novo* protein synthesis in the absence of *Stat5a-b* coupled to a defect in differentiation to downstream Tex subsets. Together, these data point to a key inability of Tex^{prog2} cells to exit quiescence, re-engage cell-cycle and transition to the Tex^{int} cell stage in the absence of *Stat5a-b*. Stat5 also mediated the transcriptional switch that accompanied this Tex^{prog2}-to- Tex^{int} transition by extinguishing some of the Tex progenitor-associated biology and fostering the effector-NK-like features that characterize the Tex^{int} subset.

Temporal reactivation of Stat5 in Tex cells drives Tex^{int} cell accumulation and synergizes with PD-L1 blockade

The key role of Stat5 for Tex^{int} cell generation suggested potential for manipulating this axis to foster development of this subset. To test this idea, we leveraged an orthogonal IL-2:IL2Rβ system to drive Stat5-signals specifically in Tex cells.[34] Point mutations in both the WT IL2Rβ and its cognate ligand, IL-2, allow the resulting orthogonal IL2Rβ (*ortho*IL2Rβ) and orthogonal IL-2 (*ortho*IL-2) to selectively interact with each-other but not with their naturally occurring counterparts.[34] Congenically distinct P14 $CD8^+$ T cells were transduced with a RV encoding the *ortho*IL2Rβ-chain (P14 IL2Rβ-ortho) or an Empty RV (P14 Empty) and co-transferred (1:1) into LCMV Cl13 infected mice (Fig. 6A). Starting on d21p.i., recipient mice received escalated doses of *ortho*IL-2 for 5 days resulting in a dose dependent expansion of the YFP^+ (RV^+) P14 IL2Rβ-ortho cells but not their P14 Empty counterparts (Fig. 6B). A numerical increase was not observed in YFP^- (RV^-) cells and, unlike WT IL-2, *ortho*IL-2 treatment also did not alter the frequency of regulatory T cells demonstrating the specificity of the *ortho*IL-2:IL2Rβ system (Fig S7A–B). Although the proportions of the different Tex subsets remained similar in the P14 Empty and endogenous $gp_{33–41}$-specific $CD8^+$ T cells (Fig. S7C–D), the P14 IL2Rβ-ortho population in the same mice displayed an expansion of Tex^{prog2} and Tex^{int} cells and concomitant reductions in the frequency of Tex^{prog1} and Tex^{term} cells with increasing doses of *ortho*IL-2 (Fig. 6C–D and S7E–G). The gradual decrease in Tex^{term} cell frequency within P14 IL2Rβ-ortho also suggested that *ortho*IL-2-mediated Stat5 activation stabilized the Tex^{int} stage, restraining

conversion to the more terminal Tex^{term} cells. Although the frequency of stem-like Tex^{prog1} cells decreased in P14 IL2Rβ-ortho, the absolute number of these key progenitor cells remained stable (Fig. S7H) suggesting that *ortho*IL-2 treatment could enhance the generation of downstream Tex subsets without depleting the Tex progenitor populations. Lastly, inducible deletion of *Stat5a-b* in Tex progenitors abrogated the impact of *ortho*IL-2 treatment on Tex^{prog} cell expansion and conversion to Tex^{int}-like cells (Fig. S7I–J). Thus, the *ortho*IL-2 system allowed temporally inducible Tex^{prog}-to-Tex^{int} conversion through Stat5.

Because expansion of Tex^{prog2} and Tex^{int} cells is also observed following PD-1:PD-L1 pathway blockade,[24] we next combined PD-1 pathway blockade with *ortho*IL-2 (Fig. 6E). P14 Empty and P14 IL2Rβ-ortho cells expanded similarly upon PD-L1 blockade in the absence of *ortho*IL2. However, the P14 IL2Rβ-ortho cells substantially outnumbered their P14 Empty counterpart in the same mice when *ortho*IL-2 was provided at the time of PD-L1 blockade (Fig. 6F–G and S7K–L). This burst in P14 IL2Rβ-ortho reflected a selective amplification of Tex^{prog2} cells and an even more robust increase in Tex^{int} cells (Fig. 6H–I). This combinatorial effect of PD-L1 blockade and *ortho*IL-2 was in contrast to minimal benefit of PD-L1 blockade in the setting of constitutive STAT5 activation from the beginning of infection (Fig. S7M). These data suggest better synergy when the induction of STAT5 activity occurred at the time of PD-1 pathway blockade. Thus, the strong combinatorial potential of IL-2-derived signals to synergize with PD-1:PD-L1 blockade reported previously[44] resides in the convergence of the two approaches at amplifying the Tex^{int} subset in a Stat5-dependent manner.

Temporal reactivation of Stat5 in Tex progenitors enables functional recovery and partial epigenetic rewiring towards the Teff-Tmem lineage upon rechallenge

Because Stat5-dependent signals restrain exhaustion and foster effector-like biology, we next tested whether engaging this axis could rewire the epigenetic program of established Tex cells. To test this idea, $Ly108^+$ Tex progenitors expressing the *ortho*-IL2Rβ were sort-purified on d27p.i. These cells were then adoptively transferred into congenic naïve recipient mice that were subsequently challenged with LCMV Arm (Fig. 7A). On day 3-to-7 post challenge (p.ch.), recipient mice received daily injections of PBS or *ortho*IL-2 (150KIU) with or without anti-PD-L1 (Fig. 7A). Responses of these donor Tex populations were compared to the recall capacity of conventional Tmem cells isolated from LCMV Arm mice (d>90p.i.). On d8p.ch, Tmem cells numerically outperformed IL2Rβ-ortho $Ly108^+$ Tex progenitors from the PBS-treated group ($Tex^{[PBS]}$) by ~54-fold (Fig. 7B). $Tex^{[PBS]}$ cells also remained poor cytokine producers, had lower expression of cytolytic molecules (i.e. Gzmb, Gzma), rapidly re-expressed Tox and PD-1, and generated few $KLRG1^+CD127^-$ secondary Teff compared to the donor Tmem cells (Fig. 7C–E). In contrast, however, IL2Rβ-ortho $Ly108^+$ Tex progenitors treated with *ortho*IL-2 ($Tex^{[oIL2]}$) during re-challenge underwent robust secondary expansion, approaching the expansion potential of Tmem cells, especially when *ortho*IL-2 was combined with PD-L1 blockade (Fig. 7B). The accumulation advantage of $Tex^{[oIL2]}$ versus $Tex^{[PBS]}$ cells persisted at d40 p.ch. (Fig. 7B - right). *Ortho*IL-2 treatment was sufficient to restore polyfunctionality as assessed by IFNγ and TNF co-production and this functionality was not further enhanced by addition of PD-L1 blockade (Fig.

7C). *Ortho*IL-2 treatment also resulted in higher expression of effector-related molecules reaching mean fluorescence intensities (MFIs) similar to (T-bet, CD94, GzmB) or even higher (GzmA) than observed for secondary Teff cell responses derived from Tmem cells and those qualitative changes occurred in the absence of an increase in the KLRG1^{+} population (Fig. 7D, E). Tox expression was reduced in Tex$^{[oIL2]}$ cells whereas PD-1 expression remained unchanged compared to Tex$^{[PBS]}$ cells (Fig. 7D), consistent with the additional benefit of blocking the PD-1 pathway in combination with *ortho*IL-2 treatment (Fig. 7B and D). Thus, in this rechallenge setting, *ortho*IL-2 treatment synergized with PD-L1 blockade for robust expansion of Tex progenitor cells and accessing the IL-2-STAT5 axis had a selective qualitative impact on expansion, polyfunctionality and effector biology.

To interrogate the mechanisms of this *ortho*IL-2 treatment benefit on Tex cells, we performed ATACseq on Tmem, Tex$^{[PBS]}$ and Tex$^{[oIL2]}$ cells at d8p.ch. PCA revealed distinct chromatin landscapes for Tmem, Tex$^{[PBS]}$ and Tex$^{[oIL2]}$ cells with 4701 DAPs (lfc>2, FDR≤0.01) by pairwise comparisons (Fig. 7F,G, Table S5). K-means clustering of all DAPs identified modules of open chromatin regions preferentially accessible in Tex^{prog} cells undergoing re-recall response (open in Tex$^{[PBS]}$ vs Tmem cells; C1 and C2; Exhaustion-Modules) or Tmem cells (open in Tmem vs Tex$^{[PBS]}$ cells; C3 and C4; Memory-Modules) (Fig. 7H, Table S5). Thus, even in settings of strong (de)differentiation signals, scars of the exhaustion epigenetic landscape persisted in re-expanded Tex^{prog} cells.[11,13] *Ortho*IL-2-signals, however, reversed parts of this epigenetic program in Tex^{prog}-derived cells (Fig. 7H; C2; Exhaustion-module “Reversed”) and even allowed for acquisition of open chromatin patterns associated with the Teff-Tmem lineage (Fig. 7H; C4; Memory module “Reacquired”). In addition, *ortho*IL-2 treatment increased accessibility at chromatin regions that were otherwise closed in both Tex$^{[PBS]}$ and Tmem-derived cells (Fig. 7H; C5; “IL2-Stat5 module”). Notably, *ortho*IL-2 treatment increased chromatin accessibility at genes related to cell proliferation (*Cdkn2b*), effector differentiation (*Id2*, *Klrb1c*) and IL-2-Stat5 responsiveness (*Il2ra*, *Cish*) (Table S5). Nevertheless, a fraction of Tex^{prog} cell-(C1; Exhaustion-module “Conserved”) and Tmem cell-(C3; Memory module “Not Re-acquired)-related open chromatin regions were not or were more moderately affected by *ortho*IL-2 treatment suggesting selectivity in the epigenetic changes triggered by the *ortho*IL-2-Stat5 axis (Fig. 7H). Together, these observations suggested opportunities to leverage the IL-2-Stat5 axis for therapeutic reprogramming of Tex cells.

We next compared the network of TF binding sites in the altered chromatin landscape of Tmem, Tex$^{[PBS]}$ and Tex$^{[oIL2]}$ cells undergoing a recall response. The open chromatin landscape of Tex$^{[PBS]}$ cells enriched in binding motifs for TCR-inducible bZIP domain-containing AP-1 family members ([C1]; i.e. *Fra1-2, JunB, BATF, Atf3* or AP-1) and High Mobility Group-TFs ([C2]; i.e. *Tcf7, Tcf3, Lef1*) and the *Tcf7*-partners Foxo1 and Eomes[45–47] (Fig. 7I). Tmem-derived cells, in contrast, enriched for T-box (i.e. *Tbx21*), ETS (i.e. *Ets1*) and Runt (i.e. *RUNX1–2*) motifs (C3 and C4), consistent with distinct transcriptional circuitry governing the Tex and Tmem lineages.[22,23,48,49] Although Tmem cells also contained accessible bZIP motifs, these motifs were located in different chromatin accessible regions compared to Tex$^{[PBS]}$ cells (C4 versus C1 respectively). These data suggested distinct wiring of TCR-dependent signals in Tex versus Tmem cells during rechallenge. *Ortho*IL-2 treatment did not alter accessibility at exhaustion-related bZIP motifs

(C1), but increased accessibility at bZIP motifs in the Teff-Tmem-related C4 and also at accessible chromatin regions preferentially enriched in the Tex$^{[oIL2]}$ cells (C5) (Fig. 7I). Thus, *ortho*IL-2, likely through Stat5 engagement, re-shaped the landscape of bZIP family TF binding sites in Tex cells during (re)differentiation. Moreover, *ortho*IL-2 treatment also selectively reversed the Tex-associated accessibility at HMG-TFs regions (C2) and re-engaged Tmem-Teff cell-related enhancers such as those for Runx-family of TFs (C4) (Fig. 7I). Together, the IL-2-Stat5-driven epigenetic changes during (re)differentiation of Tex^{prog} cells resulted in reshaping of the TF network in these cells that combined silencing or rewiring of some exhaustion-related open chromatin regions and re-engagement of some TF-binding regions associated with the Teff-Tmem lineage.

Discussion

Reversing or rewiring the epigenetic program of Tex cells remains a major goal of cancer immunotherapy.[11,13,22,50] Here, we discovered a reciprocal circuit where Stat5a antagonizes Tox and the Tox-driven Tex cell epigenetic program, fostering the acquisition of effector-like biology. In established Tex cells, boosting Stat5 activity partially rewired the Tex cell open chromatin landscape towards the Teff-Tmem lineage with a preferential ability to function at the point of developmental flexibility that occurs as Tex^{prog} cells convert to the “effector-like” Tex^{int} subset. The use of an orthogonal IL-2:IL2Rβ-pair system[34] allowed Stat5-signals to be directed exclusively to the antigen-specific CD8$^+$ T cells *in vivo* and synergized with PD-1 pathway blockade through coordinated expansion of Tex^{int} cells. These data may help explain the therapeutic benefit of IL-2 in settings of T cell exhaustion,[51,52] the combinatorial effect of IL-2 treatment with PD-1 pathway blockade,[44] and define mechanisms by which γ_c-cytokine signaling can impact CD8$^+$ T cell exhaustion. Moreover, a notable feature of manipulating Stat5 activity in Tex cells was the generation of a highly durable state of differentiation that combined features of effector biology, NK receptor expression, resistance to exhaustion, and durability in the setting of chronic antigen stimulation which together, could have considerable therapeutic benefit.

IL-2 was one of the first effective immunotherapies for cancer[52] and, can have a direct impact on Tex cells.[51,53–55] Our data now provide mechanistic explanations for these effects of IL-2. First, Stat5 antagonizes Tox and the Tox-dependent Tex epigenetic imprinting, and fosters effector-like differentiation. This Stat5 antagonism of Tox may explain the preferential impact of early Stat5-signals in settings where Tox is abundant (chronic infections, cancer) versus those that favor Teff cells (e.g. acutely resolving infections) where Tox expression is low.[7] Second, Stat5 was necessary for formation of Tex^{int} cells a finding that may explain the synergy between IL-2 and PD-1 blockade.[44,53,54] Mechanistically, Stat5 attenuated or extinguished the stem-like biology of Tex^{prog} cells to initiate exit from quiescence, cell-cycle re-entry and allow downstream Tex^{int} cell differentiation. One potential link between these events may be the mechanisms of downregulation of Tcf1 which is essential for exit from the Tex^{prog} cell state.[24,38,56] In other settings, IL-2:Stat5-signals can repress Tcf1 activity and promote cellular differentiation.[57,58] Indeed, here we found that enhancing Stat5 activity (STAT5CA) depleted Tcf1$^+$ cells and provoked a loss of Tcf1 binding sites in established Tex cells (*ortho*IL-2) whereas Stat5-deficiency trapped Tex cells at the progenitor stage. Thus, the balance between Tcf1 and Stat5 activity may be

one key regulatory node for differentiation of Tex^{prog} cells into downstream Tex subsets including Tex^{int} cells. Tox also directly restrains the transition from Tex^{prog}-to- Tex^{int} cells.[24] Thus, the Stat5-antagonism of Tox coupled to the role of this TF to mediate the epigenetic switch from exhaustion to effector-like programs also may explain the impact of Stat5 on T_{EX}^{int} cell formation. Third, Stat5 promotes the effector circuitry in Tex^{int} cells including driving expression of many effector (e.g. *GzmB*, *IFNg*, *FasL or perforin*) and NK-related genes also previously linked to Stat5 activity in other settings.[39,57,59] Hence, Stat5 not only functions to drive formation of Tex^{int} cells but also likely controls expression of some of the key genes associated with this effector-NK-like biology. Together, these observations provide rationale for developing therapeutic strategies to increase Stat5 activity in Tex cells in settings of chronic infection or cancer. In particular, the *ortho*IL-2 approach[34] may avoid for previous limitations by delivering Stat5 inducing signals only to the cells of interest.[60]

Since the discovery of the distinct epigenetic wiring of Tex cells that limits re-differentiation upon PD-1 blockade,[22,48] developing approaches to reprogram the epigenetics of Tex cells has been a major goal. Identifying such strategies, however, has proven challenging. The data presented here reveal potential opportunities for, at least partial epigenetic re-wiring of Tex cells. Tex cells can retain epigenetic “scars” in settings of disease cure and rapidly re-engage the Tex cell program upon antigenic rechallenge.[11,13,8,61] In the setting of an antigenic recall response, we found that boosting the IL-2:Stat5 signals reversed a substantial fraction of these exhaustion-associated scars and restored accessibility at open chromatin regions associated with the Tmem-Teff lineage. This partial epigenetic reprograming was sufficient to restore robust re-expansion and polyfunctionality. The exhaustion-specific open chromatin regions reversed by the IL-2:Stat5 axis were enriched for HMG-motifs especially those that could be bound by Tcf1. Tcf1 functions in activated $CD8^+$ T cells to maintain stemness at the expense of effector differentiation[45,46,56,62]. One possibility is that Tcf1 may restrain Teff features in Tex cells and the ability of Stat5 signals to repress Tcf1 activity[57,58] maybe be sufficient to relieve the Tcf1-mediated Tex^{prog} cell restraint. Coupled to an antagonism of Tox, IL-2:Stat5 signals are likely to provoke Tex cell rewiring by both fostering conversion of Tex^{prog} into Tex^{int} cells through Tcf1 antagonism and also by removing the Tox-dependent reinforcement of the Tex cell program during this Tex subset conversion.

Long-term persistence in settings of continued TCR signaling is a hallmark of Tex cells compared to Teff or Tmem cells.[14,15,38,63,64] Thus, a notable feature of constitutive Stat5a activity in antigen-specific $CD8^+$ T cells during chronic infection was the durability of this population despite the relative absence of the key regulators of Tex cell persistence, Tox and Tcf1.[6–9,28–30,65] Although there are some data suggesting a role for IL-2-signals in regulating memory $CD8^+$ T cell formation,[66] IL-2 signals also drive terminal differentiation of short-lived effector $CD8^+$ T cells and prolonged exposure to high doses of IL-2 can exacerbate Teff cell contraction in settings of acute viral infection[51,67–71]. Moreover, use of IL-2 for *in vitro* T cell expansion in settings of adoptive cell therapy (ACT) has been associated with poor engraftment and/or limited durability or anti-tumor activity of Ag-specific $CD8^+$ T cells.[58] Thus, although IL-2 fosters strong effector function, this cytokine can also drive terminal differentiation.[72,73] As a result, in settings of ACT, strategies to

temper Stat5-signals (e.g. using engineered IL-2 variants or alternate γ_c-cytokines during *in vitro* expansion)[57,58,74] have been developed to restrain terminal differentiation and support formation of a stem-like compartment with superior engraftment potential and anti-tumor activity.[36,57,58,67,68,75,76] Thus, our data on the durability benefits of STAT5CA in chronic viral infection suggest several possibilities. First, constitutively active Stat5 may function differently than prolonged exposure to IL-2. Second, enforcing Stat5-signals directly in $CD8^+$ T cells may differ from exogenous IL-2 treatment, especially in settings where the ability of T cells to transduce signals downstream of IL-2 is altered due to changes in receptor expression and/or signaling efficiency.[36,77,78] Third, continuous IL-2:Stat5 signals may provoke different effects than short-term IL-2 exposure as used in ACT protocols[58] or previous studies only providing additional IL-2 during the effector phase.[51] However, another possibility is that in the setting of continuous TCR signals that drive exhaustion, enforced Stat5 activity synergizes with other exhaustion-driven antigen-dependent survival signals. Dissecting these questions will be an important future goal to determine how Stat5 interacts with other signals and devise strategies to optimally exploit the Stat5:IL-2 pathway for enhancing immunotherapy.

In summary, we identify a role for augmented IL-2:Stat5 signals in a potential epigenetic rewiring of Tex cells and uncover the underlying molecular and cellular mechanisms for these effects. The result of increasing IL-2:Stat5 signals is an alternate differentiation state combining therapeutically useful features of both Teff and Tex cells leading to improved control of disease. The use of the *ortho*IL-2 system demonstrated that these effects are cell intrinsic to Tex cells and suggests future strategies for Stat5 targeting therapeutics including cytokine-based and engineered cellular therapy-based approaches. Future studies in humans will be necessary to understand how these molecular principles extend to more complex settings with both pre-existing Tex cells and opportunities for new T cell priming as well as role for other γ_c responsive cell types. Nevertheless, these data may provide a guide for developing and evaluating such therapies in future clinical trials.

Limitations of the study

We identified a central role for Stat5 in controlling key aspects of Tex cell biology, including Tex^{int} cell formation and also provide proof-of-concept for therapeutically manipulating this axis. There are, however, several limitations in this study. In addition to Tox, Stat5 influences multiple other pathways that could contribute its biological impact. Moreover, the upstream driver(s) of Stat5 activity in Tex cells during chronic infections and cancer remain to be identified. Whether different Stat5 inducers result in qualitatively or quantitatively different Stat5 biological activity in these settings will require additional work. Finally, although the developmental hierarchy of Tex subsets are beginning to be defined, and predictions from computational trajectory analysis can be informative, future lineage tracing studies will be necessary to fully determine how augmented Stat5 activity changes lineage relationships within the Tex cells developmental hierarchy.

STAR★METHODS

RESOURCE AVAILABILITY

Lead contact—Requests for additional information, resources and reagents should be directed to and will be fulfilled by the lead contact, E. John Wherry (wherry@pennmedicine.upenn.edu).

Materials availability—Materials from this study not subjected to specific agreements (orthogonal IL2:IL2Rβ-pair system) will be available from the Lead Contact upon request.

Data and code availability

- Sequencing data from this study have been deposited at GEO and are publicly available from the date of publication. Accession numbers are listed in the Key Resources Table.
- This paper does not report original code.
- Any additional information required to reanalyze the data reported in this paper is available from the lead contact on request.

EXPERIMENTAL MODELS AND AND STUDY PARTICIPANT DETAILS

Mice—Six-week old C57BL/6 female mice (CD45.2, Charles River, NCI) were used as recipient mice for most adoptive transfer experiments. Alternatively, six-week old C57BL/6 male or female (CD45.2, The Jackson Laboratory) mice were used as recipients for Stat5iKO experiments. P14 TCR transgenic mice expressing a TCR specific for the LCMV $D^{b}gp_{33–41}$ peptide were bred in house and backcrossed onto the C57BL/6 background. P14 $Rosa^{YFP}$ *Stat5a-b*$^{flox/flox}$ (P14 Stat5iKO) mice were generated by crossing *Stat5a-b*$^{flox/flox}$ mice (The Jackson laboratory) with P14 $Rosa^{YFP}$ mice (bred in house). Mice were maintained in a specific-pathogen-free (SPF) facility at the University of Pennsylvania. Ambient room temperature was ~21C, with humidity at 55%, and the light-dark cycle was 12h-12h. Experimental groups were not randomized with the exception of experiments involving tumor transplantation. All experiments and breeding conditions were in accordance with Institutional Animal Care and Use Committee (IACUC) guidelines for the University of Pennsylvania.

Viruses—LCMV Arm and Cl13 were grown in BHK cells at a multiplicity of 0.01 and/or 0.001 and supernatants were harvested at 48h and 60h post-infection. Viral productions were titrated using plaque assay on VERO cells as described.[100] Briefly, serial dilutions of culture supernatants containing LCMV virus (diluted in RPMI 1%FBS) were used to infect VERO cells. After ~1h incubation at 37°C 5%CO2, cells were overlaid with a pre-warmed (37°C) 1:1 mixture of 2× 199 media 10% FBS and 1% agarose (4ml per well of a 6-wells culture plate). After four days of incubation at 37°C 5%CO2, a second 2ml overlay supplemented with Neutral Red solution (1/20; Sigma Aldrich) was added and viral plaques were counted after an additionnal 12–14h incubation at 37°C 5%CO2.

METHOD DETAILS

Viral infections—Recipient mice were infected either intraperitoneally (i.p.) with LCMV Arm (2×10^5 plaque forming units [PFU]) or intravenously (i.v.) with LCMV Cl13 (4×10^6 PFU).

Cell line and tumor transplant—The $B16_{gp33}$ melanoma cell line was maintained in DMEM supplemented with 10% FBS, 1% L-glut and 1% Pen/Strep. Tumor cells cultured for less than two weeks were resuspended in cold PBS and implanted subcutaneously (5×10^5 cells in 50μl) in the flank of recipient mice using 29G1/2 syringes. Tumor size was monitored every two days using a digital caliper and mice were euthanized before tumors exceeded the volume permitted by the IACUC guidelines for the University of Pennsylvania.

Retroviral vectors—The STAT5CA construct has been described previously[36,37] and was kindly provided by Dr. Susan Kaech (The Salk Institute). The IL2Rβ-ortho construct has been described previously[34] and was obtained from Dr. Christopher K. Garcia (Stanford University) under the Material Transfer Agreement RIS#59882/00 between Stanford University, the University of Pennsylvania and the Parker Institute for Cancer Immunotherapy (PICI). Both constructs were cloned into a MSCV-IRES plasmid containing either VEX or YFP/GFP-reporters. RV particles were produced by transfection of 293T cells. Briefly, 293T cells were pre-incubated with warmed cDMEM supplemented with chloroquine (25μM; Sigma). Cells were transduced with a pCL-Eco plasmid (15μg) and MSCV-IRES expression plasmid (15μg) using Lipofectamine 3000 (ThermoFisher Scientific) for 6 hours at 37°C 5%CO2. After incubation, transduction medium was replaced with fresh cDMEM. RV supernatants were collected on day 3 and 4 of culture and titrated on NIH3T3 cells.

Adoptive T cell transfer—PBMCs containing 1×10^3 P14 $CD8^+$ T cells were adoptively transferred into recipient mice 24h prior to infection with either LCMV Arm or LCMV Cl13. For Stat5iKO experiments, P14 $Rosa^{YFP+/-}$ *Stat5a-b*$^{flox/flox}$ (P14 Stat5iKO) and their control counterpart P14 $Rosa^{YFP+/-}$ *Stat5a-b*$^{+/+}$ (both $CD45.1^+$ or $CD45.1.2^+$) were harvested from PBMCs and cultured in serum free RPMI medium containing (cre^+) or not (cre^-) 50μg/ml of tat-cre recombinase (Proteomic Core Facility-Children's Hospital of Philadelphia) for 45min at 37°C, 5%CO2. Cells were washed once in FBS then complete RPMI (cRPMI), resuspended in cold PBS and 1.5×10^3 of each were adoptively transferred into separate naïve CD45.2 recipients 24h before infection.[24] For all adoptive transfer experiments, markers associated with early T cell activation (i.e. CD69, Ly6C, PD-1, CD25, CD62L, CD127) were assessed in P14 populations before infusion into recipient mice to ensure transfer of phenotypically naïve T cells.

Retroviral (RV) transduction—RV transduction of P14 $CD8^+$ T cells was performed as described previously[83] with slight modifications. For each experiment, P14 $CD8^+$ T cells were enriched from spleens of P14 transgenic mice using EasySep^{tm} $CD8^+$ T cell isolation Kit (StemCell) and activated *in vitro* in cRPMI supplemented with αCD3 (1μg/ml), αCD28 (0.5μg/ml) antibodies and rhIL-2 (100U/ml) (PeproTech) at a seeding density of 1×10^6 cells/ml. One day post activation (~24–27h), $CD8^+$ T cells were re-suspended at a density

of 3–5×10^6 cells/ml mixed with RV supernatant containing polybrene (4μg/ml) at a 1:1 ratio (v/v) and spin-transduced 75' at 2000g 32°C. After transduction, 4ml of warmed cRPMI containing αCD3, αCD28 and rhIL2 was gently added to each well of a 6-well plate for a final volume of 6ml. Cells were incubated O/N (~16h) at 37°C, 5% CO2. The next day, transduced cells were stained for 15min with LiveDead Aqua (ThermoFisher Scientific) or Zombie NIR (BioLegend) and anti-CD8 antibodies in 1XPBS at RT, resuspended in warmed cRPMI and RV-positive cells (either VEX^+ of $YFP{:}GFP^+$) were sorted among live $CD8^+$ T cells (LiveDead Aqua or Zombie NIR^-CD8^+). For most RV experiments described, P14 cells expressing different congenic markers (CD45.1 or CD45.1.2) were used for transduction of control RVs (Empty) and RVs encoding proteins of interest (STAT5CA or IL2Rβ-ortho). The two congenically distinct P14 populations were then mixed at a 1:1 ratio in warmed PBS and injected into C57BL/6 recipients (2.5×10^4 each) infected 2 days earlier with LCMV Arm or Cl13.

Tumor experiments—C57BL/6 mice were inoculated with 5×10^5 B16 melanoma cells expressing the H2-D^b $gp_{33–41}$ peptide of the LCMV virus (B16gp_{33}). Ten days post tumor inoculation, mice were randomized and either left untreated or injected i.v. with FACs purified P14 Empty or P14 STAT5CA cells (5×10^5 each).

Cell preparation for flow cytometry and cell sorting—Spleens were mechanically disrupted onto a 70μM cell strainer using the plunger of a 3mL syringe and resuspended in 1mL of ACK red blood cell lysing buffer (Gibco) for 3 min at room temperature (RT). Cell suspensions were washed and resuspended in cRPMI supplemented with 10% FBS, 1% penn/strep, 1% L-glut, Hepes 10mM (Cell Center, UPenn), MEM non-essential amino acids 1% (Gibco), Sodium Pyruvate 1mM (Cell Center UPenn), β-mercaptoethanol (0.05mM). Bone marrow suspensions were harvested by flushing cells out of the femur and tibia of infected mice with a 29G syringe and cRPMI. Cells were then treated as above. For lungs and livers, mice were perfused with cold PBS. Lungs were cut in a petri dish, disrupted in 10 ml of RPMI (1%FBS) in the presence of Collagenase D (1×) (Roche) using a MACs dissociator (Miltenyi Biotec) and incubated for 45min at 37°C under agitation. After incubation, lung cells were disrupted a second time on a MACs dissociator (Miltenyi Biotec) and processed as above. After mechanical disruption onto a 70μM strainer, lymphocytes from livers were enriched using Percoll (GE Healthcare) density gradient separation (80%/40%), washed two times with cRPMI and processed as above. Blood samples were collected in 1ml of PBS 2mM EDTA. RPMI was added (1ml) and samples were underlaid with 1ml of Histopaque 1083 (Sigma Aldrich) for lymphocyte enrichment using density gradient concentration. Remaining red blood cells were lysed using ACK lysing buffer (Gibco) for 3min at RT. Equal numbers of cell were stained with extracellular antibodies for 30min on ice in FACs buffer (PBS 1×, 1% FBS, 2mM EDTA) in the presence of Live/Dead Fixable Aqua Cell Stain (ThermoFisher Scientific) or Zombie NIR (BioLegend). Cells were then fixed for 20 min on ice with Cytofix/Cytoperm (BD bioscience) and analyzed by flow cytometry. For cytoplasmic protein detection, cells were incubated for an additional 30min on ice in Perm/Wash buffer (BD bioscience) and stained for 1h on ice in Perm/Wash buffer (BD bioscience) containing antibodies targeting cytoplasmic proteins (active-caspase3, gzmA, gzmB, IFNγ, TNF). For TFs detection, cells

were fixed (20min) and permeabilized (30min) on ice using the Foxp3 Transcription Factor buffer set (ThermoFisher Scientific) and incubated for an hour with TF antibodies. For TFs detection in cells expressing a fluorescent reporter protein (VEX or GFP:YFP), cells were pre-fixed 5min in 2% formaldehyde (ThermoFisher Scientific) before fixation and permeabilization using the Foxp3 TF buffer set (ThermoFisher Scientific). Samples were resuspended in FACs buffer, acquired on an LSR II or BD FACSymphony and analysed with FlowJo v.10.8.0 software (Tree Star Inc).

For cell sorting *ex vivo*, $CD8^+$ T cells were enriched from total splenocytes using the EasySep^{tm} $CD8^+$ T cell isolation Kit (StemCell) (routinely >90% purity), stained on ice for 30' with relevant cocktails of antibodies and indicated populations were sorted at 4°C on an BD FACSARIA (BD Bioscience) using a 70 μM nozzle in 50% FBS RPMI. Purity was routinely >95%. For ATACseq, scRNAseq and CITEseq experiments, RV-positive or reporter expressing P14 cells (either VEX^+ or GFP:YFP^+) were sorted among LiveDead Aqua/ZombieNIR$^-$$CD8^+$$CD45.1^+$ cells and, when indicated, early Tex subsets were further discriminated using Ly108 and Tim-3. For re-challenge experiments, memory P14 cells from Arm infected mice were sorted among LiveDead Aqua$^-$$CD45.1^+$$CD45.2^-$$CD8^+$ T cells and Tex^{prog} cells were further discriminated as Ly108$^+$Cx3cr1$^-$ and, when indicated, YFP^+ (RV reporter$^+$, expressing the IL2Rβ-ortho).

Intracellular cytokine staining—Splenocytes or total $CD8^+$ T cells enriched using the EasySep^{tm} $CD8^+$ T cell isolation Kit (StemCell) ($1–2\times10^6$) were re-stimulated *in vitro* for 5h at 37°C 5% CO2 in cRPMI supplemented with GolgiStop (1/250; BD bioscience), GolgiPlug (1/500; BD bioscience) and $gp_{33–41}$ peptide (NIH, 0.4μg/ml). Cells were then washed and stained using the BD Fixation/permeabilization kit (BD Bioscience).

Antibody and cytokine treatment—Where indicated, mice were depleted of $CD4^+$ T cells using two i.p. injections of 200μL of PBS containing 200μg of monoclonal anti-CD4 antibody (clone GK1.5, BioXcell) one day prior and p.i. with LCMV Cl13. PD-L1 blockade was performed in CD4-depleted mice as described.[22] Sequential i.p. injections of 200μl of PBS with or without anti-mouse PD-L1 antibody (200μg/injection, clone 10F.9G2, BioXcell) were performed every three days between days 22 and 34. For re-challenge experiments, similar injections were performed at d0, 3 and 6 post infection with LCMV Arm. *Ortho*IL2 was infused daily (i.p) in 200μl of PBS at indicated concentrations from d21-to-25p.i; or every 2 days (100KIU) between d22 and 34 when combined to PD-L1 blockade; or on days d3-to-d7 post challenge (150KIU/injection).

Active caspase-3 and BrdU detection—Splenocytes from infected mice were incubated for 5 hours at 37°C 5%CO2 in cRPMI prior intra-cytoplasmic detection of active-caspase 3 (BD Bioscience) using BD Fixation/Permeabilization kit (BD Bioscience). Mice adoptively transferred with either P14 WT or P14 Stat5iKO were injected i.p with 2mg of BrdU at d7p.i. with LCMV Cl13 and BrdU detection in splenic P14 cells was performed one day later (d8p.i.) using a BrdU detection Kit (BD Bioscience) according to manufacturer's protocol.

Sample preparation for Cut&Run—Cut&Run was performed as previously described[101] with modifications. P14 Empty and P14 STAT5CA cells were sorted at d8p.i. with either LCMV Arm or Cl13 from recipients of two independent experiments and 0.5 to 3×10^5 cells were recovered in 1.5ml DNA LoBind Eppendorfs containing 650µl of 50%FBS RPMI. Samples were washed twice in 1ml of cold wash buffer (20mM HEPES-NaOH pH7.5, 150mM NaCl, 0.5mM Spermidine and protease inhibitor from Roche), re-suspended in 400µl (final) of wash buffer containing 20µl of BioMagplus Concanavalin A-coated magnetic beads (Bangs Laboratories) per reaction and rotated for 15min at 4°C to allow the cells to bind. Tubes were placed on a magnet stand and liquid was removed. Beads were then incubated O/N at 4°C in 250µl of antibody buffer (20mM HEPES-NaOH pH7.5, 150mM NaCl, 0.5mM Spermidine, 2mM EDTA, 0.1% digitonin and protease inhibitor from Roche) containing 2.5µl (1/100) of antibodies against H3K27ac (Active Motif) or IgG control (Cell Signalling Tech). Samples were then washed twice in 500µl of Digitonin Buffer (20mM HEPES-NaOH pH7.5, 150mM NaCl, 0.5mM Spermidine, 0.1% digitonin and protease inhibitor from Roche), resuspended in 250µl of cold Digitonin Buffer containing Protein-A micrococcal nuclease (pA-MN) and rotated at 4°C for 1h. Beads were washed twice in 1ml of cold Digitonin Buffer to remove unbound pA-MN, resuspended in 150µl of Digitonin Buffer, cooled down at 0°C on a pre-cooled metal block for 5min and incubated 30min at 0°C with $CaCl_2$ (3µl of 0.1M per sample) to initiate pA-MN digestion. Reaction was stopped by addition of 150µl of 2× stop Buffer (340mM NaCl, 20mM EDTA, 4mM EGTA, 0.02% Digitonin, 50µg/ml RNAseA and 50µg/ml Glycogen) followed by 10min incubation at 37°C to release target chromatin. Samples were then centrifuged 5min 16,000g 4°C and supernatants were transferred to new tubes. Chromatin fragments were incubated 10min at 70°C with 3µl of 10% SDS and 2.5µl of proteinase K (20mg/ml) followed by phenol/chloroform/isoamyl alcohol-based extraction according to original protocol (method B). Upper phase containing DNA was mixed with 1µl of glycogen (20mg/ml) and incubated with 750µl of cold 100% ethanol at −20°C O/N. Samples were centrifuged 30min 16,000g 4°C, rinsed once with 1ml of cold 100% ethanol and centrifuged again for 5min 16,000g 4°C to remove residual ethanol. Samples were air-dried, resuspended in 50µl of molecular grade water and stored at −20°C. DNA libraries were built using the NEBNext Ultra II DNA Library Prep Kit for Illumina (NewEngland Biolabs) with the following modifications.[102] NEBNext End Prep step was performed using 25µl of input material for a final volume of 30µl and the following adapted program (30min-20°C, 60min-50°C, Hold at 4°C). Adaptor was diluted at 1:25 and added at 1.5µl for ligation (15min-20°C) followed by addition of 1.5µl of Red USER Enzyme and additional 15min incubation at 37°C. Size selection was performed using 80µl of AMPure XP beads (Beckman Coulter) and purified DNA fragments were amplified for 14 cycles (annealing time changed to 10s). Libraries were cleaned-up with two rounds of size selection with AMPure XP beads (24µl/12µl; Beckman Coulter) eluted in 15µl of molecular grade water, and amplicons quality was assessed on a 2200 TapeStation (Agilent Technologies). Libraries were quantified by qPCR using the NEBNext Library Quant kit for Illumina (NewEngland Biolabs) according to manufacturer's protocol and pooled at equal molarity (1nM). Denatured Libraries were diluted at 1.8pM, loaded into a NextSeq 500/550 High Output Kit (75 cycles, Illumina) and paired-end sequencing was performed on a NextSeq 550 (Illumina).

Sample preparation for scRNAseq—Splenocytes from recipient mice were pooled from duplicate experiments and $CD8^+$ T cell enrichment was performed using the EasySep^{tm} $CD8^+$ T cell isolation Kit (StemCell). Enriched $CD8^+$ T cells were stained and P14 populations were sorted at 4°C in 1.5ml Eppendorf tubes containing 50% FBS RPMI as described above. Sorted samples were topped with cold PBS 0.04% BSA, centrifuged for 5' 350g at 4°C, washed two times in cold PBS and resuspended in 50–100μl of cold PBS. Samples were counted, down-sampled and an equivalent number of cells (~6300) between samples were loaded into the Chip (Chromium Next GEM Chip G) of a Chromium Next GEM Single Cell 3' Reagent Kit v3.1 (Dual Index, 10x Genomics) and run onto a Chromium Controller. Samples were then processed according to manufacturer's protocol. cDNA libraries were prepared using the Dual Index TT Set A (10× Genomics) and the number of indexing PCR cycles was adjusted to the cDNA input of each individual sample according to manufacturer's recommendations. Libraries were quantified by qPCR using a KAPA Library Quant Kit (KAPA Biosystems). Normalized libraries were pooled (2.5nM), loaded onto a NovaSeq 6000 SP Reagent Kit (100 cycles, Illumina) for a final concentration of 450pM and paired-end sequencing was performed on a NovaSeq 6000 (Illumina).

Sample preparation for CITEseq—CITEseq samples from duplicate experiments were prepared as described above (scRNAseq section) and processed according to the CITEseq protocol from the New York Center Technology Innovation Lab (https://cite-seq.com/protocols/). Briefly, enriched $CD8^+$ T cells were incubated for 10' at 4°C in Staining buffer (2%BSA/0.01% Tween in PBS) containing FcBlock (1/10 dilution; TruStain™ FcX, Biolegend) followed by a 30' incubation in Staining Buffer containing TotalSeqB antibodies against Ly108, CD69, Tim-3, PD-1, CD127, CD122, Lag-3, CD38 and KLRG1 (BioLegend) previously titrated according to manufacturer's protocol using PE-conjugated version of each antibodies. Samples were then washed, sorted as described above, down-sampled and equivalent number of cells (10^4) between samples were loaded onto the Chip (Chromium Next GEM Chip G) of a Chromium Next GEM Single Cell 3' Reagent Kit v3.1 (Dual Index, 10× Genomics) and run onto a Chromium Controller. Samples were then processed according to manufacturer's protocol. Gene expression and Cell surface Protein libraries were constructed using Dual Index TT Set A and Dual Index NT Set A (10× Genomics) respectively. Libraries were quantified by qPCR using a KAPA Library Quant Kit (KAPA Biosystems). Normalized libraries were pooled (0.23nM), diluted to 1.8pg/ml and loaded onto a NextSeq 500/550 High Output Kit v2.5 (150 cycles, Illumina) and paired-end sequencing was performed on a NextSeq 550 (Illumina).

Sample preparation for ATACseq—ATACseq sample preparation was performed as described[41] with minor modifications. Sorted cells (2-to-5×10^4) were washed twice in cold PBS and resuspended in 50μl of cold lysis buffer (10mM Tris-HCl, pH 7.4, 10mM NaCl, 3mM MgCl2 and 0.1% IGEPAL CA-630). Lysates were centrifuge (750xg, 10min, 4°C) and nuclei were resuspended in 50μl of transposition reaction mix (TD buffer [25μl], Tn5 Transposase [2.5μl], nuclease-free water [22.5μl]; (Illumina)) and incubated for 30min at 37°C. Transposed DNA fragments were purified using a Qiagen Reaction MiniElute Kit, barcoded with NEXTERA dual indexes (Illumina) and amplified by PCR for 11 cycles using NEBNext High Fidelity 2× PCR Master Mix (New England Biolabs). PCR products were

purified using a PCR Purification Kit (Qiagen) and amplified fragments size was verified on a 2200 TapeStation (Agilent Technologies) using High Sensitivity D1000 ScreenTapes (Agilent Technologies). Libraries were quantified by qPCR using a KAPA Library Quant Kit (KAPA Biosystems). Normalized libraries were pooled, diluted to 1.8pM, loaded onto a NextSeq 500/550 High Output Kit v2.5 (150 cycles, Illumina) and paired-end sequencing was performed on a NextSeq 550 (Illumina).

QUANTIFICATION AND STATISTICAL ANALYSIS

FlowSOM analysis—Compensated parameters for gated P14 Empty and P14 STAT5CA cells were exported from four individual mice co-transferred with both P14 populations and concatenated. Concatenated files were down-sampled using the FlowJo DownSampleV3 plugin for even representation or P14 Empty and P14 STAT5CA populations (15000 cells each), grouped using the t-sne function of FlowJo V10.8.0 using 12 parameters (CD44, Tbet, Tcf1, Tim-3, GzmB, Tox, Lag3, Icos, Ly108, CD39, CD127 and PD-1) and clusters were defined with the FlowSom plugin using the same parameters (Fig. 2C).

Ingenuity Pathways Analysis (IPA)—Indicated gene signatures (Table S1) were used as input to the Upstream regulator analysis part of the Core analysis using QIAGEN's Ingenuity Pathway Analysis (IPA, QIAGEN Redwood City, www.qiagen.com/ingenuity) to generate Transcription factor specific networks.

Taiji Rank Analysis—Transcription Factor Binding Site (TFBS) analysis and PageRank analysis were performed using Taiji[35] (https://taiji-pipeline.github.io/algorithm_PageRank.html) and paired ATACseq and RNAseq datasets of indicated Tex subsets (GEO accession number: GSE149879)[24] to generate TF ranks visualized as heatmap using R pheatmap package (Fig. 1C). For Fig. 1D, the fold change in Taiji score for Tex^{int} cells compared to other Tex subsets was calculated for each individual TF enriched in both the IPA analysis (Fig. 1B) and the Taiji Rank analysis (Fig. 1C).

ATACseq—Raw ATACseq FASTQ files from paired-end sequencing were processed using the script available at the following repository (https://github.com/wherrylab/jogiles_ATAC). Samples were aligned to the GRCm38/mm10 reference genome using Bowtie2. We used samtools to remove unmapped, unpaired, mitochondrial reads and ENCODE blacklist regions were also removed (https://sites.google.com/site/anshulkundaje/projects/blacklists). PCR duplicates were removed using Picard. Peak calling was performed using MACS v2 (FDR q-value 0.01). For each experiment, we combined peaks of all samples to create a union peak list and merged overlapping peaks with BedTools *merge*. The number of reads in each peak was determined using BedTools *coverage*. Differentially accessible peaks were identified following DESeq2 normalization using a lfc of 2 and FDR cut-off <0.01 (or <0.05 where indicated). Motif enrichment analysis was performed using Homer (findMotifsGenome.pl with options -mask, -size given and background [-bg] set as union peak). For peak tracks representation, bed files for each replicate were imported into the UCSC Genome browser online tool or IGV_2.10.2. Replicates for each sample were merged and each biological sample were normalized. For sample distance, a distance matrix was

calculated using the “euclidean” measure for all peak and plotted as a heatmap. Accessibility heatmaps in Fig. 3E were created using plotHeatmap function.

CUT&RUN and ChIPSeq data processing and analysis—Data qualities were checked using FastQC and MultiQC. Paired-end reads were aligned to mm10 reference genome using Bowtie2 v2.3.5 with options suggested by Skene et *al.* 2018.[101] Bam files containing uniquely mapped reads were kept using Samtools v1.1. MarkDuplicates command from Picard tools v1.96 was used to remove presumed PCR duplicates. Blacklist regions defined by ENCODE were removed, and filtered typical chromosomes were used for downstream analysis. Peaks were called on using MACS v2 using the broadPeak setting with general adjusted *p*-value cutoff of 0.05. Genes proximal to peaks were annotated against the mm10 genome using R package rGREAT. Peaks of all conditions were merged to create the final union peaks list. Read per million (RPM) normalized bigwig files to visualize binding signals were created using deepTools bamCoverage v3.3.2 with parameters --normalizeUsing CPM -bs 5 –smoothLength 20 – skipNAs. For visualization purpose, bigwig files of biological replicates were pooled using wiggletools with mean setting, median background were subtracted and bedGraphToBigWig was then applied to convert bedgraph to bigwig format. Tracks were loaded to UCSC genome browser for visualization. Published ChIPSeq data were downloaded from NCBI (GEO accession number: GSE64407 [Nfat1], GSE98654 [Nfat2], GSE100674 [Stat5]).[42,43,80] Paired-end reads were aligned to mm10 reference genome using Bowtie2 with same parameters as CUT&RUN. RPM normalized tracks were generated using deepTools bamCoverage. Some downloaded signal track files were lifted from mm9 to mm10 using UCSC tool liftOver. Local motif binding positions for *Tox* enhancers were identified using MEME FIMO with parameters –bfile –motifs, using homer database. Binding motifs with FDR<0.05 were plotted in Fig. 3J using R package ggplot2.

Single-Cell RNA sequencing (scRNAseq)—Sample demultiplexing, alignment, filtering, and creation of a UMI count matrix were performed using Cell Ranger software v.4.0.0 (10x Genomics). A Seurat object was created from the UMI count matrix using Seurat_4.0.5.[103] Cells with fewer than 200 or greater than 2500 detected genes were excluded from downstream analysis as of cells with >10% of mitochondrial gene counts. Genes which expression was detected in 3 cells or less were excluded. A total of 920 P14 Empty and 302 P14 STAT5CA cells passed filters with an average sequencing depth of 1984 genes per cell and were considered for downstream analysis. Counts were normalized by total expression in the corresponding cell using the “LogNormalize” function and default scaling factor of 10,000 to give counts per million. Top 2000 variable features were determined using the “vst” selection method. Linear dimensional reduction (PCA) was performed on scaled variable features and features from the 20 most significant PCs were used as input for unsupervised clustering using the “FindNeighbors” and “FindClusters” functions of Seurat with a resolution of 0.3. We next ran non-linear dimensional reduction (UMAP) to visualize the data. Differentially expressed genes were identified by the Seurat function “FindAllMarkers” with min.pct=0.25 and logfc.threshold=0.25 and the top 10 genes per cluster were used for creating the Heatmap using the R package “Dittoseq” (Fig. S4H). For projection of indicated gene signatures (SLEC, Exhaustion, Tox program and

Tex^{prog1}, Tex^{prog2}, Tex^{int}, Tex^{term} cells), Seurat clusters were used as features to calculate module scores of single cells using the "AddModuleScore" of Seurat_4.0.5. Module scores for each of the gene signatures were used to color the UMAP projections (Fig. S4I) or dot plots (Fig. 4F). Single-cell analysis of P14 Empty and P14 IL2Rβ-ortho cells was processed independently using similar pipeline. A total of 925 P14 Empty and 951 P14 IL2Rβ-ortho cells passed filters with an average sequencing depth of 1786 genes per cell and were considered for downstream analysis. Non-linear dimensional reduction (UMAP) was used to visualize data (Fig. S7E,F) from the 12 most significant PCs using a resolution of 0.1. For the multiomic single-cell data used in Fig. S3J–M, the Seurat object of the original study (Giles et *al.* Nat Immunol 2022)[23] was used for the UMAP representations and to depict the distribution of enhancers at the Tox locus as well as for calculating correlation scores of accessibility and gene expression.

Cellular Indexing of Transcriptomes and Epitopes by sequencing (CITEseq)— A UMI count matrix was created for P14 WT and P14 Stat5iKO cells using CellRanger 4.0.0. and the two matrixes were used to create Seurat objects. For each sample, an antibody ("adt") assay was created and added to its cognate Seurat object (WT or Stat5iKO) that were subsequently merged into one object containing rna and adt counts for each sample. Cells with fewer than 200 or greater than 2500 detected genes were excluded from downstream analysis as of cells with >12% of mitochondrial gene counts. Genes which expression was detected in 3 cells or less were excluded. A total of 4377 P14 WT and 4906 P14 Stat5iKO cells passed filters with an average sequencing depth of 1210 genes per cell and were considered for downstream analysis. Counts (rna assay) were then normalized, and the top 2000 variable features were scaled before running linear dimensional reduction (PCA). The 30 most significant PCs were used as input for unsupervised clustering using the "FindNeighbors" and "FindClusters" functions of Seurat with a resolution of 0.1. We next ran non-linear dimensional reduction (UMAP) using the rna assay to visualize Seurat clusters (Fig. 5F) or individual samples (Fig. 5G). DEGs were identified by the Seurat function "FindAllMarkers" with min.pct=0.25 and logfc.threshold=0.25 and the top 52 variable features by p.val.adj were used for creating the Heatmap (Fig. 5H). The "FindMarkers" function of Seurat was also used for cluster-wise assessment of the number of DEGs using as an input Seurat clusters (Fig. S6C) or oligo-tagged antibodies-defined populations (Fig. 5I). These oligo-tagged defined populations were delineated based on Ly108 and CD69 adt values with cut-off for positive and negative cells set up using the "FeatureScatter" function of Seurat. DEGs between oligo-tagged defined populations were presented as Volcano plots (Fig. 5J). For projection of indicated gene signatures (Tex^{prog1}, Tex^{prog2}, Tex^{int}, Tex^{term}), oligo-tagged defined populations were used as features to calculate module scores of single cells using the "AddModuleScore" of Seurat_4.0.5. Module scores for each of the gene signatures were used to color the UMAP projection (Fig. S6E) or dot plots (Fig. S6F).

Gene ontology—Gene ontology of indicated gene sets were obtained using the Metascape online tool (http://metascape.org/gp/index.html#/main/step1). Pathway enrichment analysis (GO Biological processes) was set for a minimum overlap of 3, a *p*-value cut-off of 0.01 and a minimum enrichment score of 1.5.

Quantification and Statistical analysis—Statistics on flow cytometry data were performed using unpaired or paired (co-adoptive transfer experiments) two-tailed Student's t test. For data presented as a ratio (Fig. 2D–E, 4B, 5A and 6F,I) a Wilcoxon signed rank test was performed with a hypothetical value of 1 or equal to the mean in control group (Fig. 6F,I) (GraphPad Prism v6; *p < 0.0332, **p < 0.0021, ***p < 0.0002, ****p < 0.0001). For statistics on scRNAseq data, a Pearson correlation coefficient was calculated as well as a *p* value of significance to estimate the degree of correlation between Stat5a and Tox signatures (Fig. 1F and S1F).

Supplementary Material

Refer to Web version on PubMed Central for supplementary material.

Acknowledgments

We thank all members of the Wherry Lab and Dr. Golnaz Vahedi (UPENN) for insightful discussions and comments on the manuscript as well as Dr. Susan Kaech (Salk Institute for Biological Studies) for providing the original STAT5CA constructs. This work was supported by the Parker Institute for Cancer Immunotherapy (PICI) and the National Institute of Health (NIH) grants AI155577, AI115712, AI117950, AI108545, AI082630 and CA210944 (to EJW). JC-B is a Parker Institute for Cancer Immunotherapy (PICI) Bridge fellow. S.F.N was supported by an Australia NHMRC C.J. Martin Fellowship (GNT1111469) and the Mark Foundation Momentum Fellowship. D.M. was supported through The American Association of Immunologists Intersect Fellowship Program for Computational Scientists and Immunologists and a Parker Institute for Cancer Immunotherapy (PICI) scholar fellowship. ACH was supported by NIH grants K08 CA230157 (ACH), R01 CA273018 (ACH), P50 CA174523 (ACH), P30 CA016520 (ACH), ACH was also supported by Damon Runyon Clinical Investigator Award, Doris Duke Clinical Scientist Development Award, the W.W. Smith Charitable Trust Award, and the Institute for Translational Medicine and Therapeutics of the Perelman School of Medicine, and the Pew-Stewart Stewart Scholars Program in Cancer Research. Work in the Huang Lab is funded by the Tara Miller Foundation and the Parker Institute for Cancer Immunotherapy. K-C.G received funding support from the Howard Hughes Medical Institute, NIH RO1 AI51321, the Parker Institute for Cancer Immunotherapy and the Ludwig Foundation.

Declaration of Interest

A.C.H performed consulting work for Immunai and receives research funding from B.M.S and Merck. K-C.G is the founder of Synthekine. E.J.W is a member of the Parker Institute for Cancer Immunotherapy which supported the study. E.J.W is an advisor for Coherus, Danger Bio, Marengo, Janssen, NewLimit, Pluto Immunotherapeutics, Related Sciences, Santa Ana Bio, Synthekine. E.J.W is a founder of Arsenal Biosciences.

References

1. Ramakrishna S, Barsan V, and Mackall C (2020). Prospects and challenges for use of CAR T cell therapies in solid tumors. Expert Opin Biol Ther 20, 503–516. 10.1080/14712598.2020.1738378. [PubMed: 32125191]
2. McLane LM, Abdel-Hakeem MS, and Wherry EJ (2019). CD8 T Cell Exhaustion During Chronic Viral Infection and Cancer. Annu Rev Immunol 37, 457–495. 10.1146/annurev-immunol-041015-055318. [PubMed: 30676822]
3. Collier JL, Weiss SA, Pauken KE, Sen DR, and Sharpe AH (2021). Notso-opposite ends of the spectrum: CD8(+) T cell dysfunction across chronic infection, cancer and autoimmunity. Nat Immunol 22, 809–819. 10.1038/s41590-021-00949-7. [PubMed: 34140679]
4. Wherry EJ, Blattman JN, Murali-Krishna K, van der Most R, and Ahmed R (2003). Viral persistence alters CD8 T-cell immunodominance and tissue distribution and results in distinct stages of functional impairment. J Virol 77, 4911–4927. [PubMed: 12663797]
5. Zajac AJ, Blattman JN, Murali-Krishna K, Sourdive DJ, Suresh M, Altman JD, and Ahmed R (1998). Viral immune evasion due to persistence of activated T cells without effector function. J Exp Med 188, 2205–2213. [PubMed: 9858507]

6. Yao C, Sun HW, Lacey NE, Ji Y, Moseman EA, Shih HY, Heuston EF, Kirby M, Anderson S, Cheng J, et al. (2019). Single-cell RNA-seq reveals TOX as a key regulator of CD8(+) T cell persistence in chronic infection. Nat Immunol 20, 890–901. 10.1038/s41590-019-0403-4. [PubMed: 31209400]
7. Khan O, Giles JR, McDonald S, Manne S, Ngiow SF, Patel KP, Werner MT, Huang AC, Alexander KA, Wu JE, et al. (2019). TOX transcriptionally and epigenetically programs CD8(+) T cell exhaustion. Nature 571, 211–218. 10.1038/s41586-019-1325-x. [PubMed: 31207603]
8. Alfei F, Kanev K, Hofmann M, Wu M, Ghoneim HE, Roelli P, Utzschneider DT, von Hoesslin M, Cullen JG, Fan Y, et al. (2019). TOX reinforces the phenotype and longevity of exhausted T cells in chronic viral infection. Nature 571, 265–269. 10.1038/s41586-019-1326-9. [PubMed: 31207605]
9. Scott AC, Dundar F, Zumbo P, Chandran SS, Klebanoff CA, Shakiba M, Trivedi P, Menocal L, Appleby H, Camara S, et al. (2019). TOX is a critical regulator of tumour-specific T cell differentiation. Nature 571, 270–274. 10.1038/s41586-019-1324-y. [PubMed: 31207604]
10. Seo H, Chen J, Gonzalez-Avalos E, Samaniego-Castruita D, Das A, Wang YH, Lopez-Moyado IF, Georges RO, Zhang W, Onodera A, et al. (2019). TOX and TOX2 transcription factors cooperate with NR4A transcription factors to impose CD8(+) T cell exhaustion. Proc Natl Acad Sci U S A 116, 12410–12415. 10.1073/pnas.1905675116. [PubMed: 31152140]
11. Abdel-Hakeem MS, Manne S, Beltra JC, Stelekati E, Chen Z, Nzingha K, Ali MA, Johnson JL, Giles JR, Mathew D, et al. (2021). Epigenetic scarring of exhausted T cells hinders memory differentiation upon eliminating chronic antigenic stimulation. Nat Immunol 22, 1008–1019. 10.1038/s41590-021-00975-5. [PubMed: 34312545]
12. Tonnerre P, Wolski D, Subudhi S, Aljabban J, Hoogeveen RC, Damasio M, Drescher HK, Bartsch LM, Tully DC, Sen DR, et al. (2021). Differentiation of exhausted CD8(+) T cells after termination of chronic antigen stimulation stops short of achieving functional T cell memory. Nat Immunol 22, 1030–1041. 10.1038/s41590-021-00982-6. [PubMed: 34312544]
13. Yates KB, Tonnerre P, Martin GE, Gerdemann U, Al Abosy R, Comstock DE, Weiss SA, Wolski D, Tully DC, Chung RT, et al. (2021). Epigenetic scars of CD8(+) T cell exhaustion persist after cure of chronic infection in humans. Nat Immunol 22, 1020–1029. 10.1038/s41590-021-00979-1. [PubMed: 34312547]
14. Angelosanto JM, Blackburn SD, Crawford A, and Wherry EJ (2012). Progressive loss of memory T cell potential and commitment to exhaustion during chronic viral infection. J Virol 86, 8161–8170. JVI.00889–12 [pii] 10.1128/JVI.00889-12. [PubMed: 22623779]
15. West EE, Youngblood B, Tan WG, Jin HT, Araki K, Alexe G, Konieczny BT, Calpe S, Freeman GJ, Terhorst C, et al. (2011). Tight regulation of memory CD8(+) T cells limits their effectiveness during sustained high viral load. Immunity 35, 285–298. 10.1016/j.immuni.2011.05.017. [PubMed: 21856186]
16. Ribas A, and Wolchok JD (2018). Cancer immunotherapy using checkpoint blockade. Science 359, 1350–1355. 10.1126/science.aar4060. [PubMed: 29567705]
17. Huang AC, Postow MA, Orlowski RJ, Mick R, Bengsch B, Manne S, Xu W, Harmon S, Giles JR, Wenz B, et al. (2017). T-cell invigoration to tumour burden ratio associated with anti-PD-1 response. Nature 545, 60–65. 10.1038/nature22079. [PubMed: 28397821]
18. Li H, van der Leun AM, Yofe I, Lubling Y, Gelbard-Solodkin D, van Akkooi ACJ, van den Braber M, Rozeman EA, Haanen J, Blank CU, et al. (2020). Dysfunctional CD8 T Cells Form a Proliferative, Dynamically Regulated Compartment within Human Melanoma. Cell 181, 747. 10.1016/j.cell.2020.04.017. [PubMed: 32359441]
19. Kamphorst AO, Wieland A, Nasti T, Yang S, Zhang R, Barber DL, Konieczny BT, Daugherty CZ, Koenig L, Yu K, et al. (2017). Rescue of exhausted CD8 T cells by PD-1-targeted therapies is CD28-dependent. Science 355, 1423–1427. 10.1126/science.aaf0683. [PubMed: 28280249]
20. Sade-Feldman M, Yizhak K, Bjorgaard SL, Ray JP, de Boer CG, Jenkins RW, Lieb DJ, Chen JH, Frederick DT, Barzily-Rokni M, et al. (2018). Defining T Cell States Associated with Response to Checkpoint Immunotherapy in Melanoma. Cell 175, 998–1013 e1020. 10.1016/j.cell.2018.10.038. [PubMed: 30388456]
21. Cercek A, Lumish M, Sinopoli J, Weiss J, Shia J, Lamendola-Essel M, El Dika IH, Segal N, Shcherba M, Sugarman R, et al. (2022). PD-1 Blockade in Mismatch Repair-Deficient, Locally Advanced Rectal Cancer. N Engl J Med. 10.1056/NEJMoa2201445.

22. Pauken KE, Sammons MA, Odorizzi PM, Manne S, Godec J, Khan O, Drake AM, Chen Z, Sen D, Kurachi M, et al. (2016). Epigenetic stability of exhausted T cells limits durability of reinvigoration by PD-1 blockade. Science. 10.1126/science.aaf2807.

23. Giles JR, Ngiow SF, Manne S, Baxter AE, Khan O, Wang P, Staupe R, Abdel-Hakeem MS, Huang H, Mathew D, et al. (2022). Shared and distinct biological circuits in effector, memory and exhausted CD8(+) T cells revealed by temporal single-cell transcriptomics and epigenetics. Nat Immunol 23, 1600–1613. 10.1038/s41590-022-01338-4. [PubMed: 36271148]

24. Beltra JC, Manne S, Abdel-Hakeem MS, Kurachi M, Giles JR, Chen Z, Casella V, Ngiow SF, Khan O, Huang YJ, et al. (2020). Developmental Relationships of Four Exhausted CD8(+) T Cell Subsets Reveals Underlying Transcriptional and Epigenetic Landscape Control Mechanisms. Immunity 52, 825–841 e828. 10.1016/j.immuni.2020.04.014. [PubMed: 32396847]

25. Hudson WH, Gensheimer J, Hashimoto M, Wieland A, Valanparambil RM, Li P, Lin JX, Konieczny BT, Im SJ, Freeman GJ, et al. (2019). Proliferating Transitory T Cells with an Effector-like Transcriptional Signature Emerge from PD1(+) Stem-like CD8(+) T Cells during Chronic Infection. Immunity 51, 1043–1058 e1044. 10.1016/j.immuni.2019.11.002. [PubMed: 31810882]

26. Zander R, Schauder D, Xin G, Nguyen C, Wu X, Zajac A, and Cui W (2019). CD4(+) T Cell Help Is Required for the Formation of a Cytolytic CD8(+) T Cell Subset that Protects against Chronic Infection and Cancer. Immunity 51, 1028–1042 e1024. 10.1016/j.immuni.2019.10.009. [PubMed: 31810883]

27. Sandu I, Cerletti D, Oetiker N, Borsa M, Wagen F, Spadafora I, Welten SPM, Stolz U, Oxenius A, and Claassen M (2020). Landscape of Exhausted Virus-Specific CD8 T Cells in Chronic LCMV Infection. Cell Rep 32, 108078. 10.1016/j.celrep.2020.108078. [PubMed: 32846135]

28. Im SJ, Hashimoto M, Gerner MY, Lee J, Kissick HT, Burger MC, Shan Q, Hale JS, Lee J, Nasti TH, et al. (2016). Defining CD8+ T cells that provide the proliferative burst after PD-1 therapy. Nature 537, 417–421. 10.1038/nature19330. [PubMed: 27501248]

29. Utzschneider DT, Charmoy M, Chennupati V, Pousse L, Ferreira DP, Calderon-Copete S, Danilo M, Alfei F, Hofmann M, Wieland D, et al. (2016). T Cell Factor 1-Expressing Memory-like CD8(+) T Cells Sustain the ImmuneResponse to Chronic Viral Infections. Immunity 45, 415–427. 10.1016/j.immuni.2016.07.021. [PubMed: 27533016]

30. Wu T, Ji Y, Moseman EA, Xu HC, Manglani M, Kirby M, Anderson SM, Handon R, Kenyon E, Elkahloun A, et al. (2016). The TCF1-Bcl6 axis counteracts type I interferon to repress exhaustion and maintain T cell stemness. Sci Immunol 1. 10.1126/sciimmunol.aai8593.

31. Daniel B, Yost KE, Hsiung S, Sandor K, Xia Y, Qi Y, Hiam-Galvez KJ, Black M, C JR, Shi Q, et al. (2022). Divergent clonal differentiation trajectories of T cell exhaustion. Nat Immunol 23, 1614–1627. 10.1038/s41590-022-01337-5. [PubMed: 36289450]

32. Kasmani MY, Zander R, Chung HK, Chen Y, Khatun A, Damo M, Topchyan P, Johnson KE, Levashova D, Burns R, et al. (2023). Clonal lineage tracing reveals mechanisms skewing CD8+ T cell fate decisions in chronic infection. J Exp Med 220. 10.1084/jem.20220679.

33. Chu Y, Dai E, Li Y, Han G, Pei G, Ingram DR, Thakkar K, Qin JJ, Dang M, Le X, et al. (2023). Pan-cancer T cell atlas links a cellular stress response state to immunotherapy resistance. Nat Med 29, 1550–1562. 10.1038/s41591-023-02371-y. [PubMed: 37248301]

34. Sockolosky JT, Trotta E, Parisi G, Picton L, Su LL, Le AC, Chhabra A, Silveria SL, George BM, King IC, et al. (2018). Selective targeting of engineered T cells using orthogonal IL-2 cytokine-receptor complexes. Science 359, 1037–1042. 10.1126/science.aar3246. [PubMed: 29496879]

35. Zhang K, Wang M, Zhao Y, and Wang W (2019). Taiji: System-level identification of key transcription factors reveals transcriptional waves in mouse embryonic development. Sci Adv 5, eaav3262. 10.1126/sciadv.aav3262. [PubMed: 30944857]

36. Hand TW, Cui W, Jung YW, Sefik E, Joshi NS, Chandele A, Liu Y, and Kaech SM (2010). Differential effects of STAT5 and PI3K/AKT signaling on effector and memory CD8 T-cell survival. Proc Natl Acad Sci U S A 107, 16601–016606. 10.1073/pnas.1003457107. [PubMed: 20823247]

37. Onishi M, Nosaka T, Misawa K, Mui AL, Gorman D, McMahon M, Miyajima A, and Kitamura T (1998). Identification and characterization of a constitutively active STAT5 mutant that promotes cell proliferation. Mol Cell Biol 18, 3871–3879. 10.1128/MCB.18.7.3871. [PubMed: 9632771]

38. Chen Z, Ji Z, Ngiow SF, Manne S, Cai Z, Huang AC, Johnson J, Staupe RP, Bengsch B, Xu C, et al. (2019). TCF-1-Centered Transcriptional Network Drives an Effector versus Exhausted CD8 T Cell-Fate Decision. Immunity 51, 840–855 e845. 10.1016/j.immuni.2019.09.013. [PubMed: 31606264]
39. Tripathi P, Kurtulus S, Wojciechowski S, Sholl A, Hoebe K, Morris SC, Finkelman FD, Grimes HL, and Hildeman DA (2010). STAT5 is critical to maintain effector CD8+ T cell responses. J Immunol 185, 2116–2124. 10.4049/jimmunol.1000842. [PubMed: 20644163]
40. Mitchell DM, and Williams MA (2013). Disparate roles for STAT5 in primary and secondary CTL responses. J Immunol 190, 3390–3398. 10.4049/jimmunol.1202674. [PubMed: 23440411]
41. Buenrostro JD, Giresi PG, Zaba LC, Chang HY, and Greenleaf WJ (2013). Transposition of native chromatin for fast and sensitive epigenomic profiling of open chromatin, DNA-binding proteins and nucleosome position. Nat Methods 10, 1213–1218. 10.1038/nmeth.2688. [PubMed: 24097267]
42. Martinez GJ, Pereira RM, Aijo T, Kim EY, Marangoni F, Pipkin ME, Togher S, Heissmeyer V, Zhang YC, Crotty S, et al. (2015). The transcription factor NFAT promotes exhaustion of activated CD8(+) T cells. Immunity 42, 265–278. 10.1016/j.immuni.2015.01.006. [PubMed: 25680272]
43. Klein-Hessling S, Muhammad K, Klein M, Pusch T, Rudolf R, Floter J, Qureischi M, Beilhack A, Vaeth M, Kummerow C, et al. (2017). NFATc1 controls the cytotoxicity of CD8(+) T cells. Nat Commun 8, 511. 10.1038/s41467-017-00612-6. [PubMed: 28894104]
44. West EE, Jin HT, Rasheed AU, Penaloza-Macmaster P, Ha SJ, Tan WG, Youngblood B, Freeman GJ, Smith KA, and Ahmed R (2013). PD-L1 blockade synergizes with IL-2 therapy in reinvigorating exhausted T cells. J Clin Invest 123, 2604–2615. 67008 [pii] 10.1172/JCI67008. [PubMed: 23676462]
45. Zhou X, Yu S, Zhao DM, Harty JT, Badovinac VP, and Xue HH (2010). Differentiation and persistence of memory CD8(+) T cells depend on T cell factor 1. Immunity 33, 229–240. 10.1016/j.immuni.2010.08.002. [PubMed: 20727791]
46. Delpoux A, Lai CY, Hedrick SM, and Doedens AL (2017). FOXO1 opposition of CD8(+) T cell effector programming confers early memory properties and phenotypic diversity. Proc Natl Acad Sci U S A 114, E8865–E8874. 10.1073/pnas.1618916114. [PubMed: 28973925]
47. Shan Q, Li X, Chen X, Zeng Z, Zhu S, Gai K, Peng W, and Xue HH (2021). Tcf1 and Lef1 provide constant supervision to mature CD8(+) T cell identity and function by organizing genomic architecture. Nat Commun 12, 5863. 10.1038/s41467-021-26159-1. [PubMed: 34615872]
48. Sen DR, Kaminski J, Barnitz RA, Kurachi M, Gerdemann U, Yates KB, Tsao HW, Godec J, LaFleur MW, Brown FD, et al. (2016). The epigenetic landscape of T cell exhaustion. Science. 10.1126/science.aae0491.
49. Doering TA, Crawford A, Angelosanto JM, Paley MA, Ziegler CG, and Wherry EJ (2012). Network Analysis Reveals Centrally Connected Genes and Pathways Involved in CD8(+) T Cell Exhaustion versus Memory. Immunity 37, 1130–1144. S1074–7613(12)00470–0 [pii] 10.1016/j.immuni.2012.08.021. [PubMed: 23159438]
50. Delgoffe GM, Xu C, Mackall CL, Green MR, Gottschalk S, Speiser DE, Zehn D, and Beavis PA (2021). The role of exhaustion in CAR T cell therapy. Cancer Cell 39, 885–888. 10.1016/j.ccell.2021.06.012. [PubMed: 34256903]
51. Blattman JN, Grayson JM, Wherry EJ, Kaech SM, Smith KA, and Ahmed R (2003). Therapeutic use of IL-2 to enhance antiviral T-cell responses in vivo. Nat Med 9, 540–547. 10.1038/nm866 nm866 [pii]. [PubMed: 12692546]
52. Rosenberg SA (2014). IL-2: the first effective immunotherapy for human cancer. J Immunol 192, 5451–5458. 10.4049/jimmunol.1490019. [PubMed: 24907378]
53. Hashimoto M, Araki K, Cardenas MA, Li P, Jadhav RR, Kissick HT, Hudson WH, McGuire DJ, Obeng RC, Wieland A, et al. (2022). PD-1 combination therapy with IL-2 modifies CD8(+) T cell exhaustion program. Nature 610, 173–181. 10.1038/s41586-022-05257-0. [PubMed: 36171288]
54. Codarri Deak L, Nicolini V, Hashimoto M, Karagianni M, Schwalie PC, Lauener L, Varypataki EM, Richard M, Bommer E, Sam J, et al. (2022). PD-1-cis IL-2R agonism yields better effectors from stem-like CD8(+) T cells. Nature 610, 161–172. 10.1038/s41586-022-05192-0. [PubMed: 36171284]

55. Beltra JC, Bourbonnais S, Bedard N, Charpentier T, Boulange M, Michaud E, Boufaied I, Bruneau J, Shoukry NH, Lamarre A, and Decaluwe H (2016). IL2Rbeta-dependent signals drive terminal exhaustion and suppress memory development during chronic viral infection. Proc Natl Acad Sci U S A 113, E5444–5453. 10.1073/pnas.1604256113. [PubMed: 27573835]
56. Shan Q, Hu S, Chen X, Danahy DB, Badovinac VP, Zang C, and Xue HH (2021). Ectopic Tcf1 expression instills a stem-like program in exhausted CD8(+) T cells to enhance viral and tumor immunity. Cell Mol Immunol 18, 1262–1277. 10.1038/s41423-020-0436-5. [PubMed: 32341523]
57. Mo F, Yu Z, Li P, Oh J, Spolski R, Zhao L, Glassman CR, Yamamoto TN, Chen Y, Golebiowski FM, et al. (2021). An engineered IL-2 partial agonist promotes CD8(+) T cell stemness. Nature 597, 544–548. 10.1038/s41586-021-03861-0. [PubMed: 34526724]
58. Hinrichs CS, Spolski R, Paulos CM, Gattinoni L, Kerstann KW, Palmer DC, Klebanoff CA, Rosenberg SA, Leonard WJ, and Restifo NP (2008). IL-2 and IL-21 confer opposing differentiation programs to CD8+ T cells for adoptive immunotherapy. Blood 111, 5326–5333. blood-2007-09-113050 [pii] 10.1182/blood-2007-09-113050. [PubMed: 18276844]
59. Grange M, Verdeil G, Arnoux F, Griffon A, Spicuglia S, Maurizio J, Buferne M, Schmitt-Verhulst AM, and Auphan-Anezin N (2013). Active STAT5 regulates T-bet and eomesodermin expression in CD8 T cells and imprints a T-bet-dependent Tc1 program with repressed IL-6/TGF-beta1 signaling. J Immunol 191, 3712–3724. 10.4049/jimmunol.1300319. [PubMed: 24006458]
60. Kalbasi A, Siurala M, Su LL, Tariveranmoshabad M, Picton LK, Ravikumar P, Li P, Lin JX, Escuin-Ordinas H, Da T, et al. (2022). Potentiating adoptive cell therapy using synthetic IL-9 receptors. Nature 607, 360–365. 10.1038/s41586-022-04801-2. [PubMed: 35676488]
61. Utzschneider DT, Gabriel SS, Chisanga D, Gloury R, Gubser PM, Vasanthakumar A, Shi W, and Kallies A (2020). Early precursor T cells establish and propagate T cell exhaustion in chronic infection. Nat Immunol 21, 1256–1266. 10.1038/s41590-020-0760-z. [PubMed: 32839610]
62. Danilo M, Chennupati V, Silva JG, Siegert S, and Held W (2018). Suppression of Tcf1 by Inflammatory Cytokines Facilitates Effector CD8 T Cell Differentiation. Cell Rep 22, 2107–2117. 10.1016/j.celrep.2018.01.072. [PubMed: 29466737]
63. Wherry EJ, Barber DL, Kaech SM, Blattman JN, and Ahmed R (2004). Antigen-independent memory CD8 T cells do not develop during chronic viral infection. Proc Natl Acad Sci U S A 101, 16004–16009. 0407192101 [pii] 10.1073/pnas.0407192101. [PubMed: 15505208]
64. Shin H, Blackburn SD, Blattman JN, and Wherry EJ (2007). Viral antigen and extensive division maintain virus-specific CD8 T cells during chronic infection. J Exp Med 204, 941–949. jem.20061937 [pii] 10.1084/jem.20061937. [PubMed: 17420267]
65. Siddiqui I, Schaeuble K, Chennupati V, Fuertes Marraco SA, Calderon-Copete S, Pais Ferreira D, Carmona SJ, Scarpellino L, Gfeller D, Pradervand S, et al. (2019). Intratumoral Tcf1(+)PD-1(+)CD8(+) T Cells with Stem-like Properties Promote Tumor Control in Response to Vaccination and Checkpoint Blockade Immunotherapy. Immunity 50, 195–211 e110. 10.1016/j.immuni.2018.12.021. [PubMed: 30635237]
66. Williams MA, Tyznik AJ, and Bevan MJ (2006). Interleukin-2 signals during priming are required for secondary expansion of CD8+ memory T cells. Nature 441, 890–893. nature04790 [pii] 10.1038/nature04790. [PubMed: 16778891]
67. Pipkin ME, Sacks JA, Cruz-Guilloty F, Lichtenheld MG, Bevan MJ, and Rao A (2010). Interleukin-2 and inflammation induce distinct transcriptional programs that promote the differentiation of effector cytolytic T cells. Immunity 32, 79–90. S1074–7613(10)00010–5 [pii] 10.1016/j.immuni.2009.11.012. [PubMed: 20096607]
68. Kalia V, Sarkar S, Subramaniam S, Haining WN, Smith KA, and Ahmed R (2010). Prolonged interleukin-2Ralpha expression on virus-specific CD8+ T cells favors terminal-effector differentiation in vivo. Immunity 32, 91–103. S1074–7613(10)00008–7 [pii] 10.1016/j.immuni.2009.11.010. [PubMed: 20096608]
69. Mathieu C, Beltra JC, Charpentier T, Bourbonnais S, Di Santo JP, Lamarre A, and Decaluwe H (2015). IL-2 and IL-15 regulate CD8+ memory T-cell differentiation but are dispensable for protective recall responses. Eur J Immunol 45, 3324–3338. 10.1002/eji.201546000. [PubMed: 26426795]
70. Boulet S, Daudelin JF, and Labrecque N (2014). IL-2 Induction of Blimp-1 Is a Key In Vivo Signal for CD8+ Short-Lived Effector T Cell Differentiation. J Immunol. 10.4049/jimmunol.1302365.

71. Mitchell DM, Ravkov EV, and Williams MA (2010). Distinct roles for IL-2 and IL-15 in the differentiation and survival of CD8+ effector and memory T cells. J Immunol 184, 6719–6730. jimmunol.0904089 [pii] 10.4049/jimmunol.0904089. [PubMed: 20483725]
72. Liao W, Lin JX, and Leonard WJ (2013). Interleukin-2 at the crossroads of effector responses, tolerance, and immunotherapy. Immunity 38, 13–25. 10.1016/j.immuni.2013.01.004. [PubMed: 23352221]
73. Spolski R, Li P, and Leonard WJ (2018). Biology and regulation of IL-2: from molecular mechanisms to human therapy. Nat Rev Immunol 18, 648–659. 10.1038/s41577-018-0046-y. [PubMed: 30089912]
74. Shourian M, Beltra JC, Bourdin B, and Decaluwe H (2019). Common gamma chain cytokines and CD8 T cells in cancer. Semin Immunol 42, 101307. 10.1016/j.smim.2019.101307. [PubMed: 31604532]
75. Gattinoni L, Zhong XS, Palmer DC, Ji Y, Hinrichs CS, Yu Z, Wrzesinski C, Boni A, Cassard L, Garvin LM, et al. (2009). Wnt signaling arrests effector T cell differentiation and generates CD8+ memory stem cells. Nat Med 15, 808–813. 10.1038/nm.1982. [PubMed: 19525962]
76. Shin HM, Kapoor V, Guan T, Kaech SM, Welsh RM, and Berg LJ (2013). Epigenetic modifications induced by Blimp-1 Regulate CD8(+) T cell memory progression during acute virus infection. Immunity 39, 661–675. 10.1016/j.immuni.2013.08.032. [PubMed: 24120360]
77. Gong D, and Malek TR (2007). Cytokine-dependent Blimp-1 expression in activated T cells inhibits IL-2 production. J Immunol 178, 242–252. 178/1/242 [pii]. [PubMed: 17182561]
78. Martins GA, Cimmino L, Liao J, Magnusdottir E, and Calame K (2008). Blimp-1 directly represses Il2 and the Il2 activator Fos, attenuating T cell proliferation and survival. J Exp Med 205, 1959–1965. 10.1084/jem.20080526. [PubMed: 18725523]
79. Bengsch B, Ohtani T, Khan O, Setty M, Manne S, O'Brien S, Gherardini PF, Herati RS, Huang AC, Chang KM, et al. (2018). Epigenomic-Guided Mass Cytometry Profiling Reveals Disease-Specific Features of Exhausted CD8 T Cells. Immunity 48, 1029–1045 e1025. 10.1016/j.immuni.2018.04.026. [PubMed: 29768164]
80. Villarino AV, Sciume G, Davis FP, Iwata S, Zitti B, Robinson GW, Hennighausen L, Kanno Y, and O'Shea JJ (2017). Subset- and tissue-defined STAT5 thresholds control homeostasis and function of innate lymphoid cells. J Exp Med 214, 2999–3014. 10.1084/jem.20150907. [PubMed: 28916644]
81. Joshi NS, Cui W, Chandele A, Lee HK, Urso DR, Hagman J, Gapin L, and Kaech SM (2007). Inflammation directs memory precursor and short-lived effector CD8(+) T cell fates via the graded expression of T-bet transcription factor. Immunity 27, 281–295. S1074–7613(07)00371–8 [pii] 10.1016/j.immuni.2007.07.010. [PubMed: 17723218]
82. Rouillard AD, Gundersen GW, Fernandez NF, Wang Z, Monteiro CD, McDermott MG, and Ma'ayan A (2016). The harmonizome: a collection of processed datasets gathered to serve and mine knowledge about genes and proteins. Database (Oxford) 2016. 10.1093/database/baw100.
83. Kurachi M, Kurachi J, Chen Z, Johnson J, Khan O, Bengsch B, Stelekati E, Attanasio J, McLane LM, Tomura M, et al. (2017). Optimized retroviral transduction of mouse T cells for in vivo assessment of gene function. Nat Protoc 12, 1980–1998. 10.1038/nprot.2017.083. [PubMed: 28858287]
84. Ewels P, Magnusson M, Lundin S, and Kaller M (2016). MultiQC: summarize analysis results for multiple tools and samples in a single report. Bioinformatics 32, 3047–3048. 10.1093/bioinformatics/btw354. [PubMed: 27312411]
85. Langmead B, and Salzberg SL (2012). Fast gapped-read alignment with Bowtie 2. Nat Methods 9, 357–359. 10.1038/nmeth.1923. [PubMed: 22388286]
86. Li H, Handsaker B, Wysoker A, Fennell T, Ruan J, Homer N, Marth G, Abecasis G, Durbin R, and Genome Project Data Processing, S. (2009). The Sequence Alignment/Map format and SAMtools. Bioinformatics 25, 2078–2079. 10.1093/bioinformatics/btp352. [PubMed: 19505943]
87. Quinlan AR, and Hall IM (2010). BEDTools: a flexible suite of utilities for comparing genomic features. Bioinformatics 26, 841–842. 10.1093/bioinformatics/btq033. [PubMed: 20110278]

88. Ramirez F, Ryan DP, Gruning B, Bhardwaj V, Kilpert F, Richter AS, Heyne S, Dundar F, and Manke T (2016). deepTools2: a next generation web server for deep-sequencing data analysis. Nucleic Acids Res 44, W160–165. 10.1093/nar/gkw257. [PubMed: 27079975]

89. Zerbino DR, Johnson N, Juettemann T, Wilder SP, and Flicek P (2014). WiggleTools: parallel processing of large collections of genome-wide datasets for visualization and statistical analysis. Bioinformatics 30, 1008–1009. 10.1093/bioinformatics/btt737. [PubMed: 24363377]

90. Zhang Y, Liu T, Meyer CA, Eeckhoute J, Johnson DS, Bernstein BE, Nusbaum C, Myers RM, Brown M, Li W, and Liu XS (2008). Model-based analysis of ChIP-Seq (MACS). Genome Biol 9, R137. 10.1186/gb-2008-9-9-r137. [PubMed: 18798982]

91. Kent WJ, Sugnet CW, Furey TS, Roskin KM, Pringle TH, Zahler AM, and Haussler D (2002). The human genome browser at UCSC. Genome Res 12, 996–1006. 10.1101/gr.229102. [PubMed: 12045153]

92. Heinz S, Benner C, Spann N, Bertolino E, Lin YC, Laslo P, Cheng JX, Murre C, Singh H, and Glass CK (2010). Simple combinations of lineage-determining transcription factors prime cis-regulatory elements required for macrophage and B cell identities. Mol Cell 38, 576–589. 10.1016/j.molcel.2010.05.004. [PubMed: 20513432]

93. Grant CE, Bailey TL, and Noble WS (2011). FIMO: scanning for occurrences of a given motif. Bioinformatics 27, 1017–1018. 10.1093/bioinformatics/btr064. [PubMed: 21330290]

94. Gu Z, and Hubschmann D (2023). rGREAT: an R/bioconductor package for functional enrichment on genomic regions. Bioinformatics 39. 10.1093/bioinformatics/btac745.

95. Zhu LJ, Gazin C, Lawson ND, Pages H, Lin SM, Lapointe DS, and Green MR (2010). ChIPpeakAnno: a Bioconductor package to annotate ChIP-seq and ChIP-chip data. BMC Bioinformatics 11, 237. 10.1186/1471-2105-11-237. [PubMed: 20459804]

96. Huber W, Carey VJ, Gentleman R, Anders S, Carlson M, Carvalho BS, Bravo HC, Davis S, Gatto L, Girke T, et al. (2015). Orchestrating high-throughput genomic analysis with Bioconductor. Nat Methods 12, 115–121. 10.1038/nmeth.3252. [PubMed: 25633503]

97. Gentleman RC, Carey VJ, Bates DM, Bolstad B, Dettling M, Dudoit S, Ellis B, Gautier L, Ge Y, Gentry J, et al. (2004). Bioconductor: open software development for computational biology and bioinformatics. Genome Biol 5, R80. 10.1186/gb-2004-5-10-r80. [PubMed: 15461798]

98. Zhou Y, Zhou B, Pache L, Chang M, Khodabakhshi AH, Tanaseichuk O, Benner C, and Chanda SK (2019). Metascape provides a biologist-oriented resource for the analysis of systems-level datasets. Nat Commun 10, 1523. 10.1038/s41467-019-09234-6. [PubMed: 30944313]

99. Hao Y, Hao S, Andersen-Nissen E, Mauck WM 3rd, Zheng S, Butler A, Lee MJ, Wilk AJ, Darby C, Zager M, et al. (2021). Integrated analysis of multimodal single-cell data. Cell 184, 3573–3587 e3529. 10.1016/j.cell.2021.04.048. [PubMed: 34062119]

100. Welsh RM, and Seedhom MO (2008). Lymphocytic choriomeningitis virus (LCMV): propagation, quantitation, and storage. Curr Protoc Microbiol Chapter 15, Unit 15A 11. 10.1002/9780471729259.mc15a01s8.

101. Skene PJ, Henikoff JG, and Henikoff S (2018). Targeted in situ genome-wide profiling with high efficiency for low cell numbers. Nat Protoc 13, 1006–1019. 10.1038/nprot.2018.015. [PubMed: 29651053]

102. Cao Z, Budinich KA, Huang H, Ren D, Lu B, Zhang Z, Chen Q, Zhou Y, Huang YH, Alikarami F, et al. (2021). ZMYND8-regulated IRF8 transcription axis is an acute myeloid leukemia dependency. Mol Cell 81, 3604–3622 e3610. 10.1016/j.molcel.2021.07.018. [PubMed: 34358447]

103. Butler A, Hoffman P, Smibert P, Papalexi E, and Satija R (2018). Integrating single-cell transcriptomic data across different conditions, technologies, and species. Nat Biotechnol 36, 411–420. 10.1038/nbt.4096. [PubMed: 29608179]

Highlights

- Stat5-signals direct Tex^{int} cell formation and instigate effector-NK biology
- STAT5CA restrains Tox, opposes exhaustion and achieves a durable effector-like state
- Boosting Stat5 in Tex cells enhances Tex^{int} cells and amplifies responses to αPD-L1
- Accessing Stat5 in Tex^{prog} cells partially reverses exhaustion and restores functions

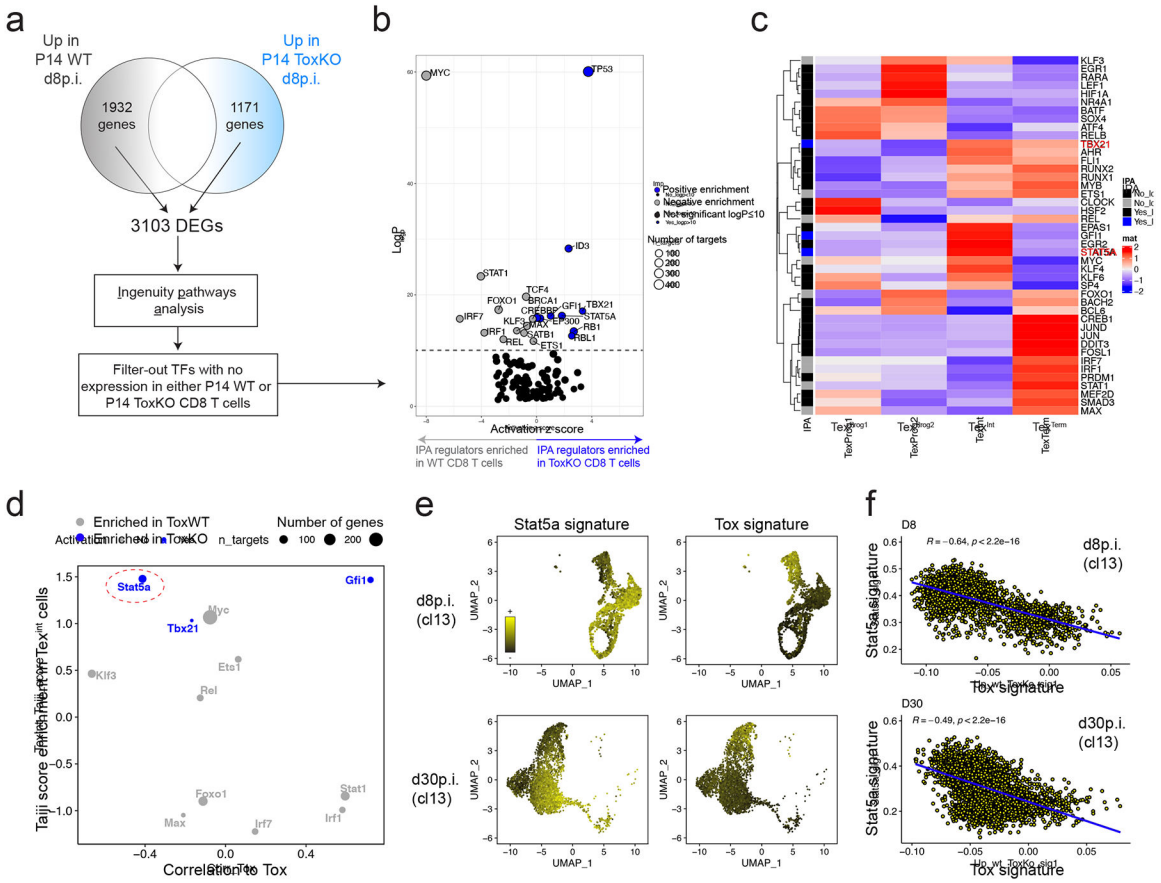

Figure 1: Stat5a and Tox are reciprocally active and oppositely regulated in Ag-specific CD8$^+$ T cells during chronic infection.

A- Ingenuity pathways analysis (IPA) was performed on differentially expressed genes (DEGs; *p*val≤0.05) between WT and ToxKO CD8$^+$ T cells (Table. S1).[7] **B-** Transcriptional regulators identified by IPA and enriched in WT (grey) or ToxKO (blue) CD8$^+$ T cells. Non-significant hits are colored in black. Bubble size represents the number of genes considered by the IPA for each TF (Table. S1). **C-** Taiji rank analysis[35] identifying TFs with increased activity in indicated subsets based on published RNAseq and ATACseq data.[24] Plotted are overlapping TFs identified in both the IPA analysis in Fig. 1B and the independent Taiji analysis. **D-** IPA regulators enriched from Fig. 1B (logp≥10) and in the independent Taiji Rank analysis in Fig. 1C were plotted based on their fold change in Taiji enrichment for Tex^{int} cells (Y-axis) and correlation of the IPA-defined gene network for each TF to Tox expression (X-axis). **E-** UMAP of re-processed scRNAseq of LCMV-specific P14 CD8$^+$ T cells at d8 (upper panel)[38] or d30 (lower panel)[11] post LCMV clone 13 (Cl13) infection. Module scores for a Stat5a network (defined by the IPA; left) or Tox signature (right; genes enriched in P14 WT versus P14 ToxKO)[7] were used to color the UMAP. **F-** Correlation scores between Stat5a network and a Tox signature[7] at indicated time of Cl13 infection. Please see also Figure S1 and Table S1.

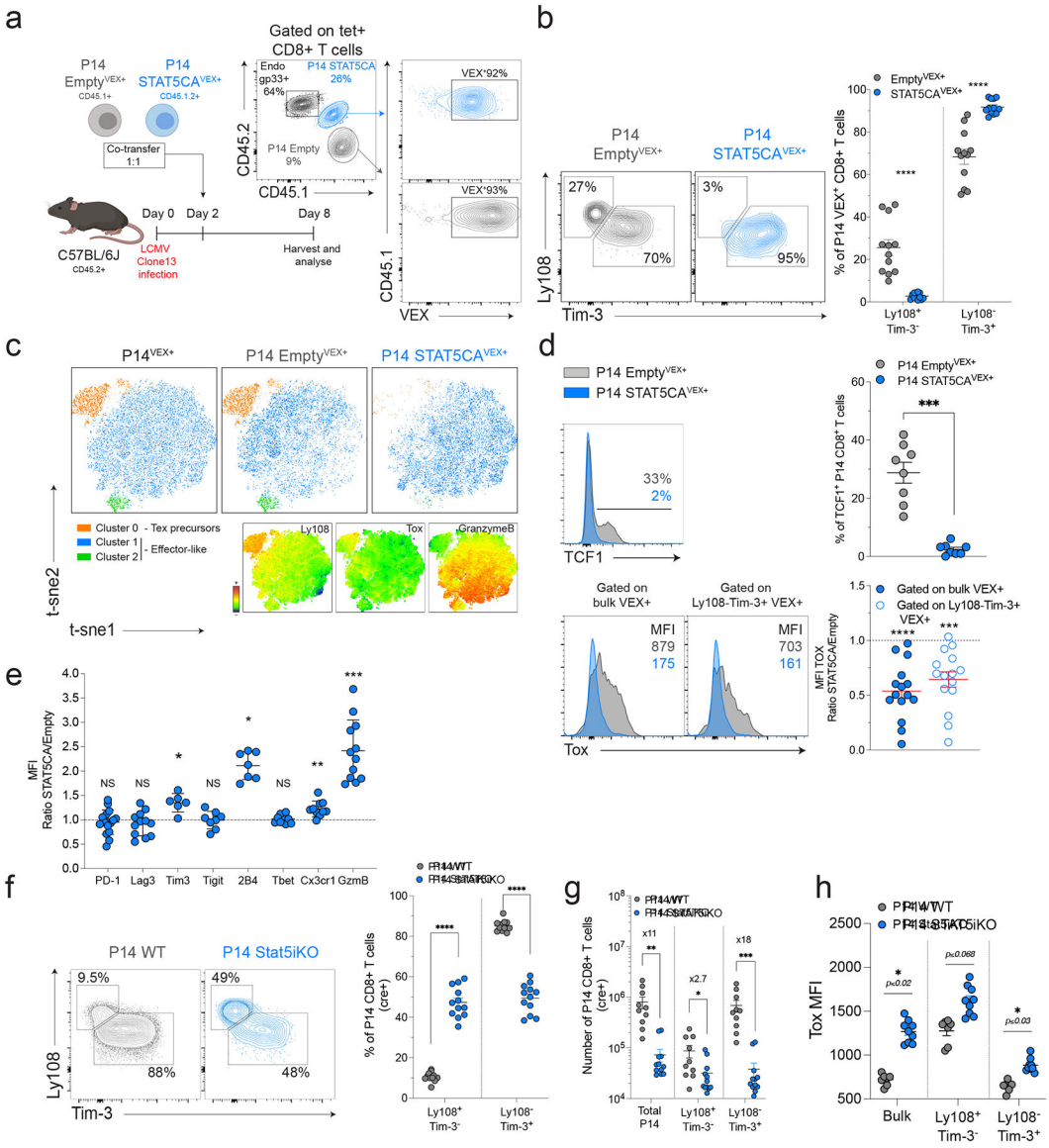

Figure 2: Stat5 opposes Tox and antagonizes establishment of exhaustion.

A- Experimental design. **B-** Frequency of Ly108-Tim-3-defined subsets in indicated RV$^+$ (Violet-excited positive [VEX$^+$]) populations at d8p.i. **C-** t-sne representation of flow cytometry data highlighting FlowSOM clusters for bulk VEX$^+$ P14 cells (left), P14 Empty^{VEX+} (middle) and P14 STAT5CA^{VEX+} (right) (see methods). **D-** Tcf1 and Tox expression in indicated RV$^+$ (VEX$^+$) populations at d8p.i. **E-** MFI of indicated markers (ratio P14 STAT5CA/P14 Empty). **F-** Frequency of Ly108-Tim-3-defined subsets in indicated YFP$^+$ (cre$^+$) populations at d8p.i. **G-** Absolute numbers of indicated YFP$^+$ (cre$^+$) populations at d8p.i. **H-** Tox expression in indicated sub-populations of YFP$^+$ (cre$^+$) P14 WT and P14 Stat5iKO at d8p.i.

(**B**) N=3 independent experiments (ind exp) with 12 mice per group (**D**) N=2 (Tcf1) or 4 (Tox) with 8 (Tcf1) or 15 (Tox) mice per group (**E**) N=2–4 ind exp with 6–16 mice per group (**F-G**) N=3 ind exp with 10–12 mice per group (**H**) N=2 with 7–9 mice per group.

Mean ± SEM shown. For statistical analysis, paired (**B, D**) or unpaired (**F-H**) two-tailed Student's t test were performed. A Wilcoxon signed rank test was performed for **E** with a hypothetical value of 1. *p < 0.0332, **p < 0.0021, ***p < 0.0002, ****p < 0.0001. Please see also Figure S2.

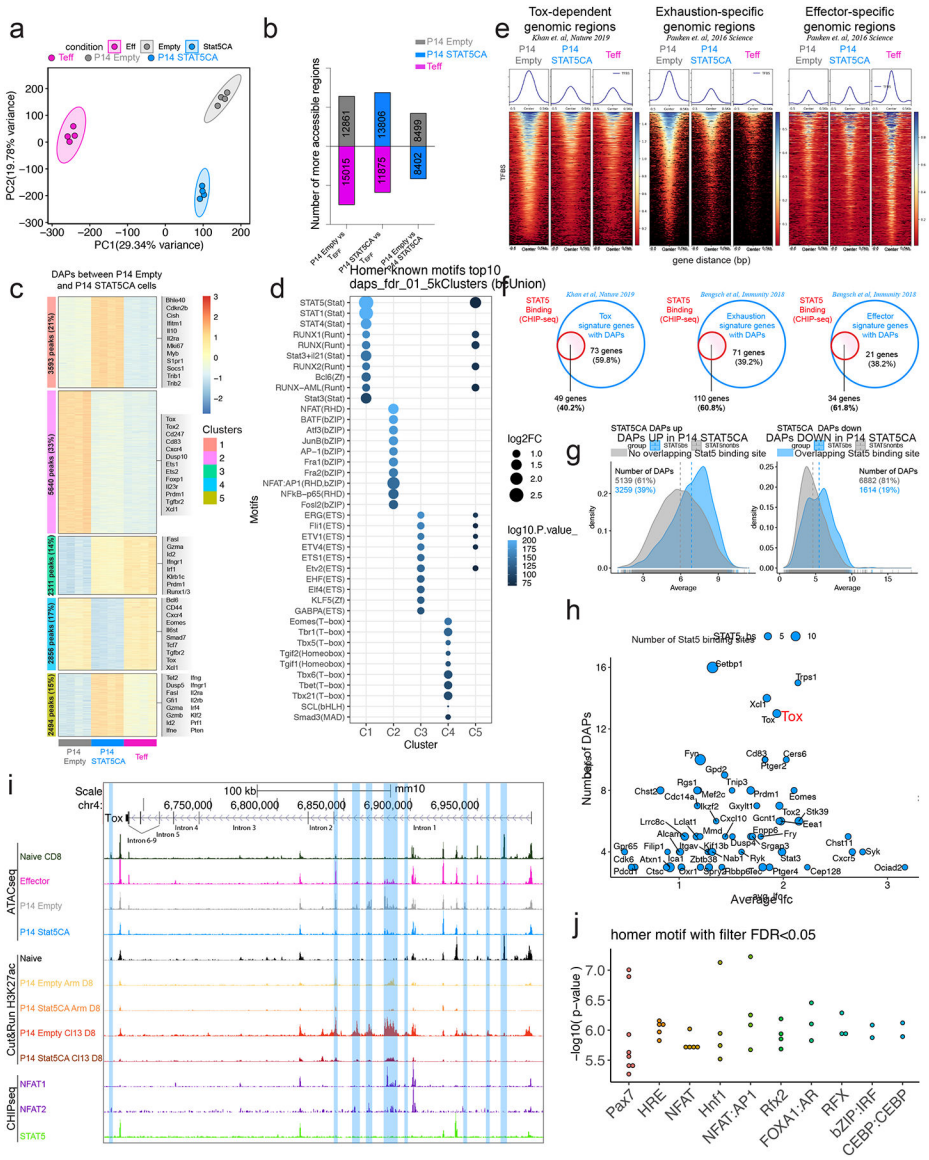

Figure 3: Enhanced Stat5a activity restrains Tox and the exhaustion program while supporting an effector epigenetic landscape.

Splenic P14 Empty and P14 STAT5CA cells isolated at d8 of Cl13 infection were analyzed by ATACseq. Naïve (not depicted) and P14 CD8$^+$ T cells isolated from Arm infected mice at d8p.i. were used as reference. **A**- PCA of normalized ATACseq counts (top 500 DAPs). **B**- Number of peaks more accessible in indicated populations and comparisons (FDR 0.01, lfc≥2). **C**- Clustered heatmap (k-means) of DAPs between P14 Empty and P14 STAT5CA. **D**- Top 10 motifs (Homer) enriched in DAPs from corresponding clusters in Fig.3C. **E**- Heatmap of accessibility for indicated populations at Tox-related enhancers (more accessible in ToxWT versus ToxKO P14 CD8$^+$ T cells; left)[7] or genomic regions more accessible in Tex (versus naïve, Teff and Tmem; middle) or Teff (versus naïve, Tex and Tmem) cells (FDR 0.01, lfc>3; Table S2).[22] **F**- Frequency of genes from indicated signature gene lists[7,79] (Table S2) with DAPs between P14 Empty and P14 STAT5CA that possess direct binding sites for Stat5 (based on published CHIPseq).[80] **G**- Average change in accessibility of DAPs

between P14 Empty and P14 STAT5CA that overlapped (blue) or not (grey) with a Stat5 binding site.[80] **H**- Dot plot of exhaustion signature genes[79] containing at least 3 DAPs between P14 Empty and P14 STAT5CA cells and scored by the number of DAPs per gene (Y-axis), average lfc (X-axis) and number of Stat5 binding sites (bubble size)[80]. **I**- ATACseq, Cut&Run (H3K27ac) and CHIPseq (NFAT1,[42] NFAT2[43] and Stat5[80]) tracks at the *Tox* locus. Blue highlights indicate ATAC peaks reduced in P14 STAT5CA cells compared to P14 Empty. **J**- Top 10 local motif (homer) at *Tox* enhancers (FDR<0.05).
Please see also Figure S3 and Table S2.

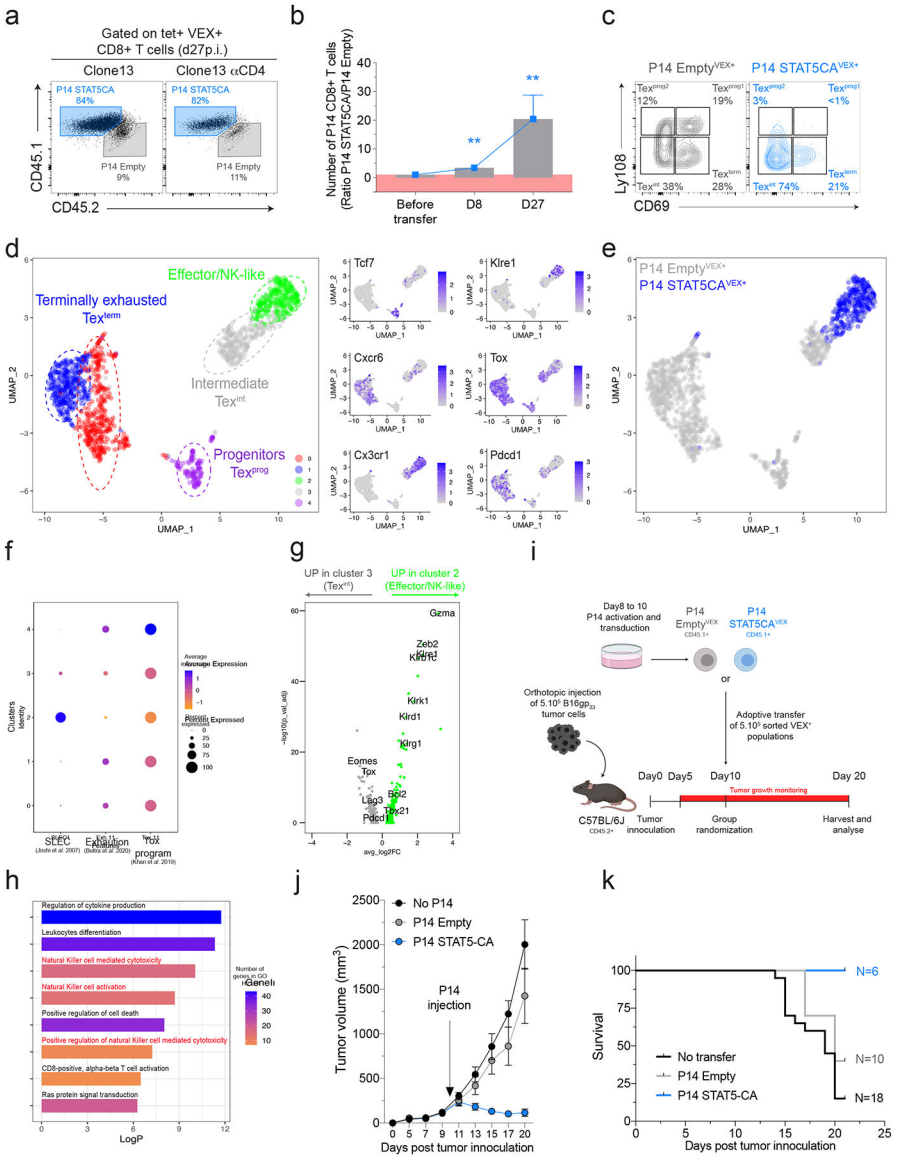

Figure 4: Constitutive Stat5a activity drives a stable and protective effector-NK-like CD8$^+$ T cell differentiation state during chronic viral infection and cancer.

A- Frequency of co-transferred P14 Empty and P14 STAT5CA cells among RV$^+$ (violet excited fluorescent protein [VEX$^+$]) CD8$^+$ T cells at d27p.i. with Cl13 (left) or Cl13 with CD4-depletion (right). **B-** Ratio of cell number (P14 STAT5CA/P14 Empty) at indicated time points in the spleen. **C-** Frequency of Ly108-CD69-defined subsets in indicated populations of VEX$^+$ cells at d27p.i. **D-E** UMAP of scRNAseq data combining P14 Empty^{VEX+} and P14 STAT5CA^{VEX+} cells isolated at d27p.i. plotting Seurat clusters (**D-left**), samples (**E**) or selected genes **(D-right). F-** Module scores for indicated signatures in Seurat clusters from Fig. 4D. **G-** DEGs (log2FC>0.25, p_value_adj≤0.05) between C2 and C3 from Fig. 4D. **H-** Gene ontology for genes Up in C2 vs C3 from Fig. 4D. **I-** Experimental design. **J-K-** B16$_{gp33}$ tumor growth **(J)** and Kaplan Meyer survival curve **(K)** for each experimental group.

(**A**) Representative of 2 ind exp with 10 mice per group (**B**) N=4 ind exp with 16–21 mice per time points (**C**) Representative of 2 ind exp with 9–10 mice per group (**J-K**) Representative of 2 ind exp with at least 6 mice per group in each. Mean ± SEM shown. For statistical analysis, a Wilcoxon signed rank test was performed with a hypothetical value of 1 (**B**). **p < 0.0021.

Please see also Figure S4 and Table S3.

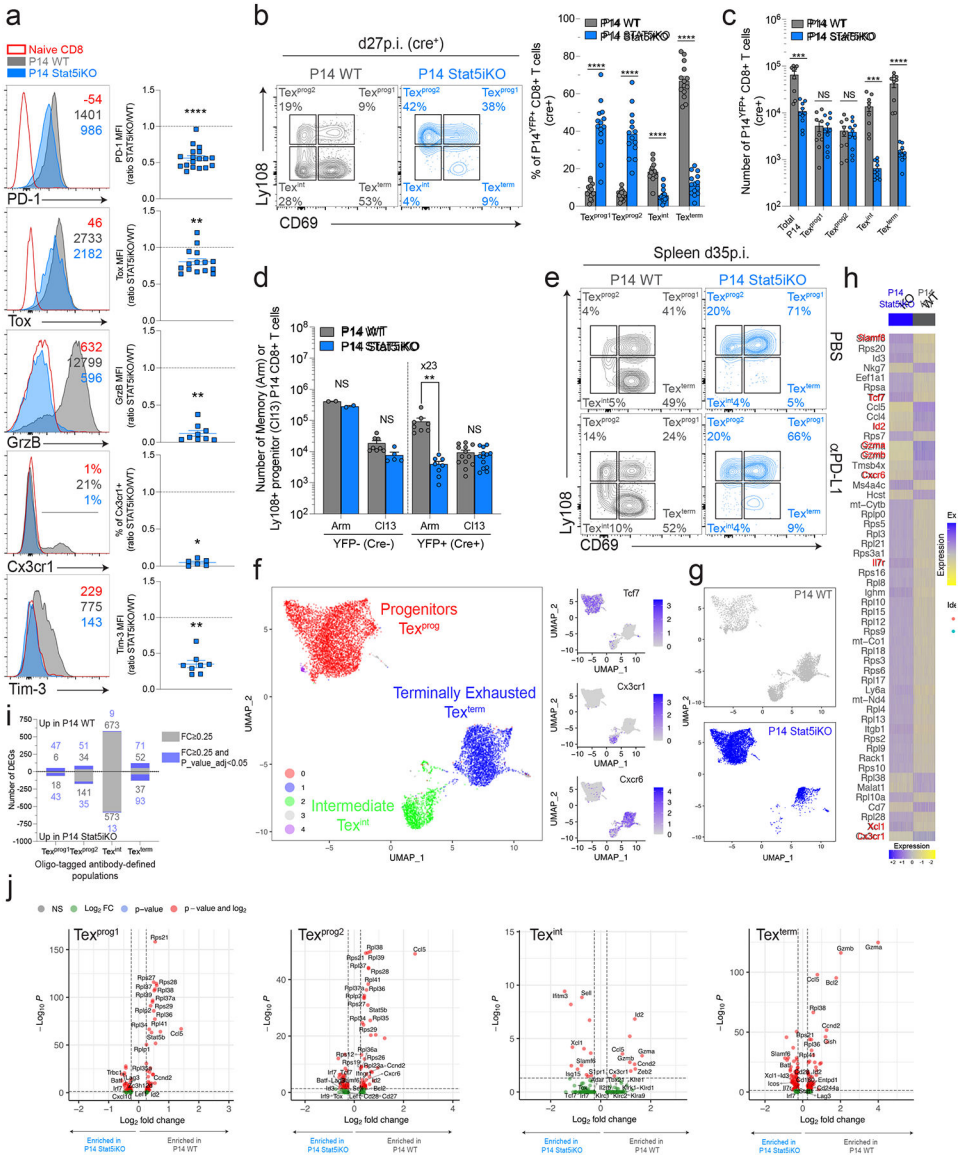

Figure 5: Stat5-signals drive Tex^{int} cell development and are essential for CD8^{+} T cell responses to PD-L1 blockade.

A- Expression of key markers on indicated splenic populations at d27p.i. **B-C** Frequency (**B**) and absolute number (**C**) of Ly108 and CD69-defined subsets among indicated yellow fluorescent protein positive (YFP^{+}, cre^{+}) populations of P14 Empty and P14 Stat5iKO at d27p.i. **D-** Absolute numbers of Tmem and Ly108^{+} Tex^{prog} cells in indicated P14 populations at d27 post Arm (memory) or Cl13 (Ly108^{+} progenitors) infection with (YFP^{+}cre^{+}) or without (YFP^{-}cre^{-}) *in vitro* treatment with tat-cre recombinase prior to adoptive transfer. **E-** Frequency of Ly108 and CD69-defined subsets among YFP^{+} (cre^{+}) P14 WT and P14 Stat5iKO cells at d35p.i. in CD4^{+} T cell-sdepleted hosts treated (αPD-L1) or not (PBS) with anti-PD-L1 antibodies (see methods). **F-G-** UMAP plotting RNA-defined Seurat clusters (**F**-left) or samples (**G**) from CITEseq analysis of P14 WT and P14 Stat5iKO cells isolated at d27p.i. **H-** Top DEGs between P14 WT and P14 Stat5iKO. **I-** Number of DEGs between oligo-tagged antibodies (Ly108 and CD69)-defined populations (see Fig.

S6D,E). **J**- DEGs (FC≥0.25) between indicated oligo-tagged antibodies (Ly108 and CD69)-defined populations of P14WT and P14 Stat5iKO cells.
(**A**) N=2–5 ind exp with 6–18 mice per group (**B**) N=4 ind exp with 14 mice per group (**C**) N=3 ind exp with 9–10 mice per group (**D**) N=1–2 ind exp with 2–8 mice per group (**E**) Representative of 2 ind exp with 8–10 mice per group. Mean ± SEM shown. For statistical analysis, unpaired (**B-D**) two-tailed Student's t tests were performed. A Wilcoxon signed rank test was performed for **A** with a hypothetical value of 1. *p < 0.0332, **p < 0.0021, ***p < 0.0002, ****p < 0.0001.
Please see also Figure S5, S6 and Table S4.

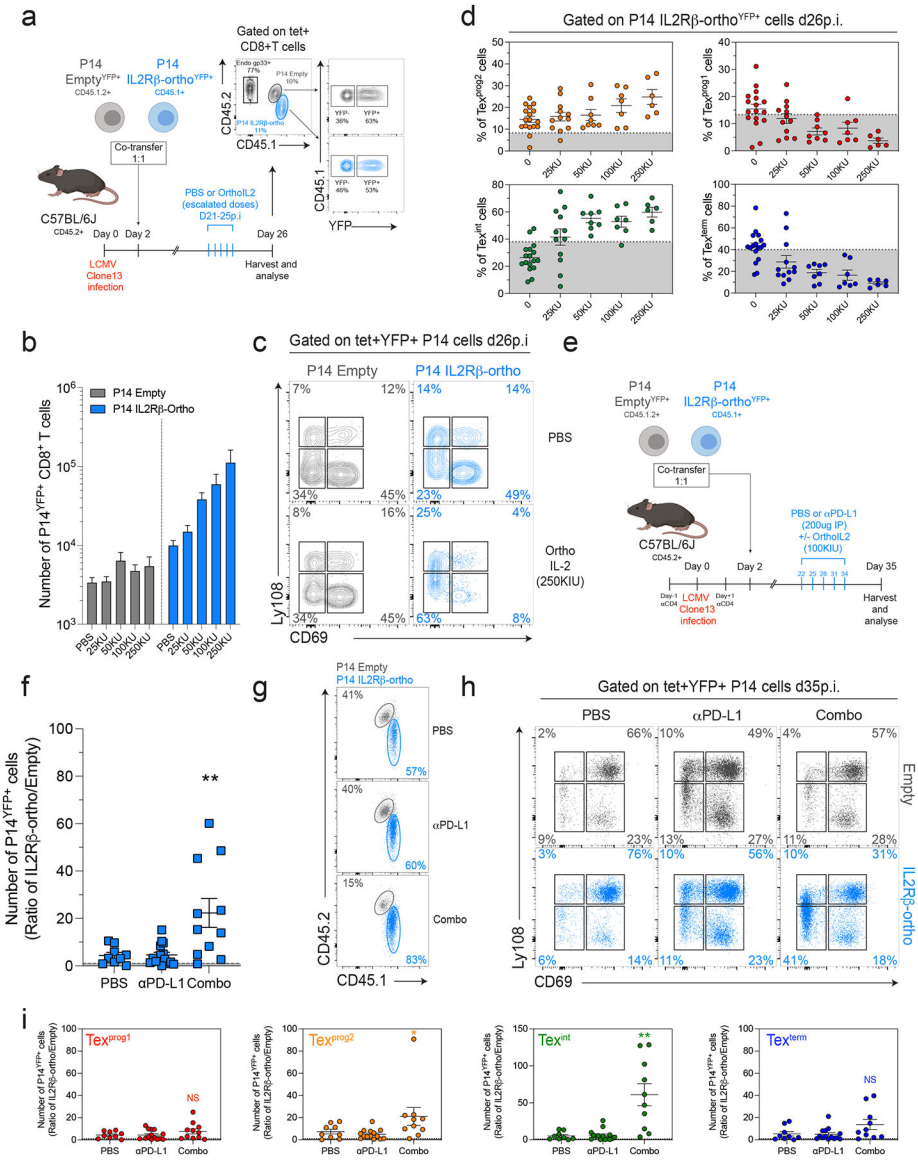

Figure 6: Orthogonal IL-2:IL2Rβ-triggered Stat5 activation in Ag-specific CD8^{+} T cells enforces Tex^{int} cell development and synergizes with PD-L1 blockade.

A- Experimental design. **B**- Absolute numbers of yellow fluorescent protein positive (YFP^{+}) P14 Empty and P14 IL2Rβ-ortho cells isolated at d26p.i. from experimental groups infused with indicated concentration of *ortho*IL-2. **C**- Frequency of Ly108 and CD69-defined subsets among co-transferred P14 Empty^{YFP+} and P14 IL2Rβ-ortho^{YFP+} cells isolated at d26p.i. from indicated experimental groups. **D**- Frequency of indicated subsets among P14 IL2Rβ-ortho^{YFP+} cells isolated at d26p.i. from experimental groups infused with indicated concentrations of *ortho*IL-2. Dotted grey lines indicate mean frequencies of each sub-population across all experimental groups in P14 IL2Rβ-ortho^{YFP-} control cells. **E**- Experimental design. **F**-**G** Ratio of cell number (P14 IL2Rβ-ortho^{YFP+}/P14 Empty^{YFP+}) (**F**) and relative frequency (**G**) of P14 Empty^{YFP+} and P14 IL2Rβ-ortho^{YFP+} cells in indicated experimental groups at d35p.i. Combo stands for αPD-L1+*ortho*IL-2 (100KIU). **H**- Frequency of Ly108 and CD69-defined subsets among P14 Empty^{YFP+} and P14 IL2Rβ-

ortho^{YFP+} cells isolated at d35p.i. from indicated experimental groups. **I**- Ratio of cell number between indicated subsets of P14 IL2Rβ-ortho^{YFP+}/P14 Empty^{YFP+} in indicated experimental groups at d35p.i.

(**B**) N=2 ind exp with 6–10mice per group (**C**) N=2 with 6 mice per group (**D**) N=2 with 6–17 mice per group (**F-I**) N=2 with 9–15 mice per group. Mean ± SEM shown. For statistical analysis, a Wilcoxon signed rank test was performed for with a hypothetical value equal to the mean in control (PBS) group (**F, I**). *p < 0.0332, **p < 0.0021.

Please see also Figure S7.

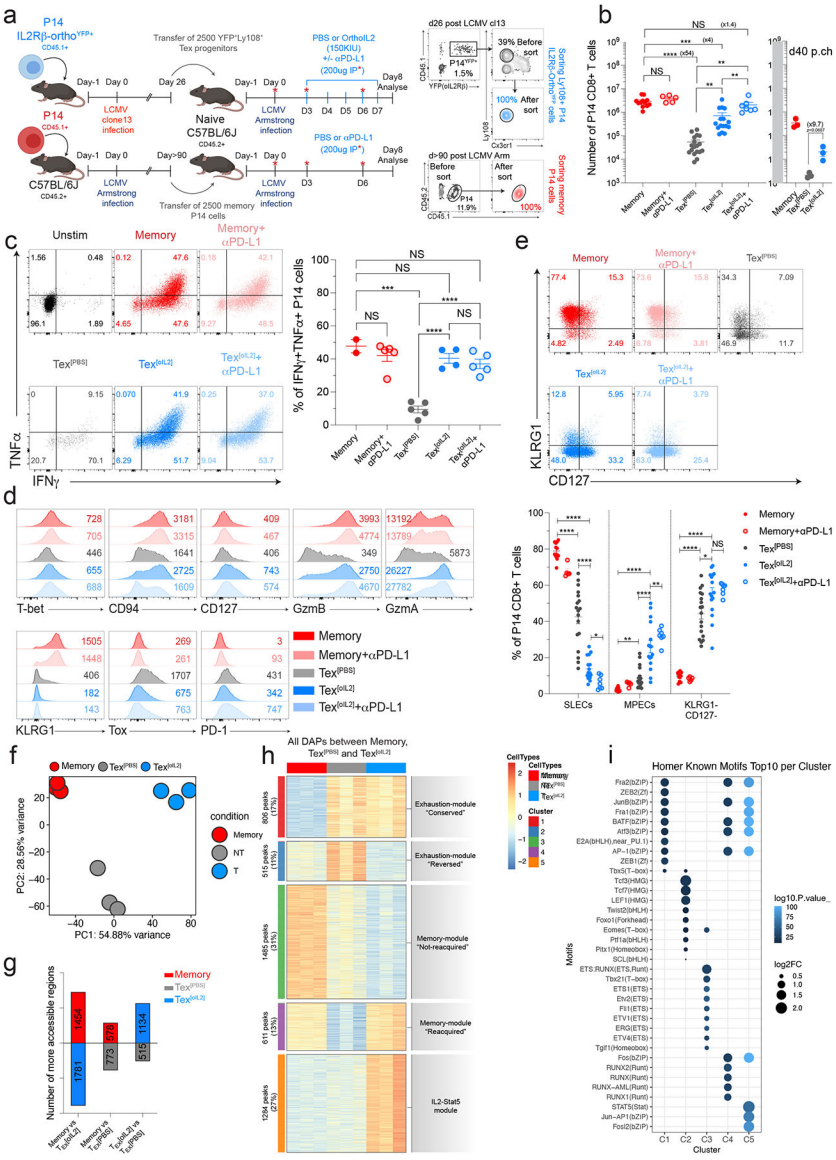

Figure 7: Targeted IL-2-Stat5 signals on rechallenged Tex^{prog} provokes a partial epigenetic rewiring of these cells and improves function.

A- Experimental design. P14 Memory (Memory) and P14 Ly108^{+} Tex progenitors expressing the IL2Rβ-ortho receptor (yellow fluorescent protein positive [YFP^{+}], Tex) were sorted from indicated time post Arm (d≥90p.i.) or Cl13 (d26p.i.) infection respectively (see sorting strategy – right panel), transferred into new hosts (2.5×10^{3} each) and challenged with LCMV Arm. Mice injected with Tex cells (Ly108^{+} P14 expressing IL2Rβ-ortho^{YFP+}) were treated with either PBS (Tex$^{[PBS]}$) or daily infusion of *ortho*IL-2 (150KIU day 3–7; [Tex$^{[oIL2]}$) in combination or not with αPD-L1 blockade (day0, −3 and −6p.ch.). P14 memory cells were treated with PBS or αPD-L1 at similar time points. Cells were analyzed in the spleen at d8p.ch. **B**- Absolute numbers in the spleen at d8 (left) and 40 p.ch. (right). **C**- Cytokine secretion after 5h of *in vitro* re-stimulation with gp33 peptide. **D**- MFI of indicated markers on re-challenged memory and Tex cells from each experimental condition. **E**- Frequency of KLRG1 and CD127-defined sub-populations among re-challenged memory

and Tex cells from indicated experimental groups. **F**- PCA of normalized ATACseq counts (top 500 DAPs). **G**- Number of peaks more accessible in indicated populations and comparisons (FDR 0.01, lfc≥2). **H**- Clustered heatmap (k-means) plotting all DAPs between indicated populations (Table S5). **I**- Motif enrichment analysis (Homer) plotting the top 10 motifs enriched in DAPs from corresponding clusters in Fig.7H.
(**B**) N=5 with 5–18 mice per group (**C**) Representative of 2 ind exp with 2–8 mice per group (**D**) Representative of 5 ind exp with 5–18 mice per group (**E**) N=5 with 5–18 mice per group. Mean ± SEM shown. For statistical analysis, unpaired (**B, C, E**) two-tailed Student's t tests were performed. *p < 0.0332, **p < 0.0021, ***p < 0.0002, ****p < 0.0001.
Please see also Table S5.

KEY RESOURCE TABLE

REAGENT or RESOURCE	SOURCE	IDENTIFIER
Antibodies		
FITC mouse anti-mouse CD244 (clone 2B4)	BD Biosciences	Cat# 553305 RRID:AB_394769
FITC Hamster anti-mouse KLRG1 (clone 2F1)	SouthernBiotech	Cat# 1807-02 RRID:AB_2795367
Alexa Fluor 488 anti-mouse Ly-6C (clone HK1.4)	Biolegend	Cat# 128022 RRID:AB_10639728
PE/Dazzle 594 anti-mouse TIGIT (clone 1G9)	Biolegend	Cat# 142110 RRID:AB_2566573
PE-CF594 rat anti-mouse CD127 (clone SB/199)	BD Biosciences	Cat# 562419 RRID:AB_11153131
PE-Cyanine 5 anti-mouse/rat ICOS (clone C398.4A)	Ebioscience	Cat# 15-9949-82 RRID:AB_468828
PE/Cy5 anti-mouse CD69 (clone H1.2F3)	Biolegend	Cat# 104510 RRID:AB_313113
PE/Cy7 anti-mouse CD279 (PD-1, clone RMP1-30)	Biolegend	Cat# 109110 RRID:AB_572017
PE anti-mouse Ly108 (clone 330-AJ)	Biolegend	Cat# 134606 RRID:AB_2188095
APC anti-mouse CD223 (Lag-3, clone eBioC9B7W)	Ebioscience	Cat# 17-2231-82 RRID:AB_2573184
Alexa Fluor 647 anti-mouse/human CD44 (clone IM7)	Biolegend	Cat# 103018 RRID:AB_493681
APC-eFluor 780 anti-mouse CD62L (clone MEL-14)	Ebioscience	Cat# 47-0621-82 RRID:AB_1603256
APC-eFluor 780 anti-mouse KLRG1 (clone 2F1)	Ebioscience	Cat# 47-5893-82 RRID:AB_2573988
BD OptiBuild BUV395 Rat Anti-Mouse CD44 (clone IM7)	BD Biosciences	Cat# 740215 RRID:AB_2739963
APC-Cy7 rat anti-mouse CD25 (clone PC61)	BD Biosciences	Cat# 557658 RRID:AB_396773
APC-Cy7 rat anti-mouse CD19 (clone 1D3)	BD Biosciences	Cat# 557655 RRID:AB_396770
APC-eFluor 780 anti-mouse CD4 (clone RM4-5)	Ebioscience	Cat# 47-0042-82 RRID:AB_1272183
Alexa Fluor 700 anti-mouse CD45.1 (clone A20)	Biolegend	Cat# 110724 RRID:AB_493733
Brillant Violet 785 anti-mouse CD45.1 (clone A20)	Biolegend	Cat# 110743 RRID:AB_2563379
eFluor 450 anti-mouse CD223 (Lag-3, clone eBioC9B7W)	Ebioscience	Cat# 48-2231-82 RRID:AB_11149866
Pacific Blue anti-mouse Ly108 (clone 330-AJ)	Biolegend	Cat# 134608 RRID:AB_2188093
Brillant Violet 605 anti-mouse CD4 (clone RM4-5)	Biolegend	Cat# 100548 RRID:AB_2563054
Brillant Violet 605 anti-mouse CX3CR1 (clone SA011F1)	Biolegend	Cat# 149027 RRID:AB_2565937

REAGENT or RESOURCE	SOURCE	IDENTIFIER
APC anti-mouse CX3CR1 (clone SA011F1)	Biolegend	Cat# 149008 RRID:AB_2564492
Brillant Violet 605 anti-mouse CD366 (Tim-3, clone RMT3-23)	Biolegend	Cat# 119721 RRID:AB_2616907
Brillant Violet 650 anti-mouse CD8a (clone 53-6.7)	Biolegend	Cat# 100742 RRID:AB_2563056
Brillant Violet 785 anti-mouse CD45.2 (clone 104)	Biolegend	Cat# 109839 RRID:AB_2562604
Alexa Fluor 700 anti-mouse CD45.2 (clone 104)	Biolegend	Cat# 109822 RRID:AB_493731
Purified anti-mouse CD16/32 Antibody	Biolegend	Cat#101302 RRID:AB_312801
BD Horizon BUV737 rat anti-mouse CD127 (clone SB/199)	BD Biosciences	Cat# 612841 RRID:AB_2870163
APC/Fire 750 anti-mouse CD279 (PD-1, clone 29F.1A12)	Biolegend	Cat# 135239 RRID:AB_2629767
BD OptiBuild BUV496 rat anti-mouse CD4 (clone RM4-4)	BD Biosciences	Cat# 741051 RRID:AB_2870666
APC anti-mouse CD94 (clone 18d3)	Biolegend	Cat# 105512 RRID:AB_2721459
Ultra-LEAF purified anti-mouse CD28 (clone 37.51)	Biolegend	Cat# 102116 RRID:AB_11147170
LEAF purified anti-mouse CD3s (clone 145-2C11)	Biolegend	Cat# 100331 RRID:AB_1877073
TotalSeq™-B0003 anti-mouse CD366 (Tim-3, clone RMT3-23) Antibody	Biolegend	Cat# 119741 RRID:AB_2832425
TotalSeq™-B0004 anti-mouse CD279 (PD-1) Antibody	Biolegend	Cat# 109125 RRID:AB_2819818
TotalSeq™-B0197 anti-mouse CD69 Antibody	Biolegend	Cat# 104555 RRID:AB_2832336
TotalSeq™-B0198 anti-mouse CD127 (IL-7Ra) Antibody	Biolegend	Cat# 135055 RRID:AB_2860677
TotalSeq™-B0227 anti-mouse CD122 (IL-2RP) Antibody	Biolegend	Cat# 105913 RRID:AB_2860611
TotalSeq™-B0378 anti-mouse CD223 (LAG-3) Antibody	Biolegend	Cat# 125245 RRID:AB_2860661
TotalSeq™-B0557 anti-mouse CD38 Antibody	Biolegend	Cat# 102739 RRID:AB_2876403
TotalSeq™-B0250 anti-mouse/human KLRG1 (MAFA) Antibody	Biolegend	Cat# 138435 RRID:AB_2860688
TotalSeq™-B0563 anti-mouse CX3CR1 Antibody	Biolegend	Cat# 149045 RRID:AB_2888877
TotalSeq™-B0930 anti-mouse Ly108 Antibody	Biolegend	Cat# 134615 RRID:AB_2892288
FITC mouse anti-Ki67 (clone B56)	BD Biosciences	Cat# 556026 RRID:AB_396302
FITC anti-T-bet (clone 4B10)	Biolegend	Cat# 644812 RRID:AB_2200540
Anti-Human Granzyme B PE-Texas Red (clone GB11)	Invitrogen	Cat# GRB17 RRID:AB_2536540

REAGENT or RESOURCE	SOURCE	IDENTIFIER
PE Rabbit anti-active Caspase-3 (clone C92-605)	BD Biosciences	Cat# 550914 RRID:AB_393957
PE mouse anti-TCF-7/TCF-1 (clone S33-966)	BD Biosciences	Cat# 564217 RRID:AB_2687845
PE-Cy7 anti-mouse TNFa (clone MP6-XT22)	Ebioscience	Cat# 25-7321-82 RRID:AB_11042728
APC anti-mouse IFNg (clone XMG1.2)	Ebioscience	Cat# 17-7311-82 RRID:AB_469504
APC anti-TOX human and mouse (clone REA473)	Miltenyi Biotech	Cat# 130-118-335 RRID:AB_2751485
Anti-mouse Granzyme A PE-Cyanine7 (clone GzA-3G8.5)	Invitrogen	Cat# 25-5831-82 RRID:AB_2573476
Anti-mouse Eomes PE-Cy7 (clone Dan11Mag)	Invitrogen	Cat# 25-4875-82 RRID:AB_2573454
PE anti-mouse FOXP3 (clone MF-14)	Biolegend	Cat # 126404 RRID:AB_1089117
Histone H3K27ac antibody pAb	Active Motif	Cat# 39034
Rabbit (DA1E) mAb IgG XP Isotype control	Cell Signaling Tech	Cat# 3900S
In vivo Mab anti-mouse CD4 (clone GK1.5)	BioXcell	Cat# BE0003-1
In vivo Mab anti-mouse PD-L1 (clone 10F.9G2)	BioXcell	Cat# BE0101
Bacterial and Virus Strains		
LCMV clone 13	Rafi Ahmed	N/A
LCMV Armstrong (Arm)	Rafi Ahmed	N/A
Chemicals, Peptides, and Recombinant Proteins		
Live/Dead Fixable Aqua Dead cell stain Kit	ThermoFisher Scientific	Cat# L34957
Zombie NIR Fixable viability kit	Biolegend	Cat# 423105
Recombinant Murine IL-2	Peprotech	Cat#212-12
ACK Lysing Buffer	ThermoFisher Scientific	Cat#A1049201
Deoxyribonuclease I from bovine pancreas	Sigma-Aldrich	Cat#D5025
Collagenase D	Roche	Cat#11088866001
Golgi Stop	BD Biosciences	Cat#554724
Golgi Plug	BD Biosciences	Cat#555029
gp (33–41) peptide KAVYNFATM	GenScript	Custom
LCMV tetramers (gp33)	NIH	N/A
Percoll®	Sigma-Aldrich	Cat#GE17-0891-01
Histopaque®−1083	Sigma-Aldrich	Cat#10831
Tat-cre Recombinase	Protein and Proteomics Core Facility, The Children's Hospital of Philadelphia	N/A
Paraformaldehyde 16% solution, EM grade	Electron Microscopy Sciences	Cat# 15710
NEBNext High-Fidelity 2X PCR Master Mix	New England Biolabs	Cat#M0541
Orthogonal IL-2	Dr. K. Christopher Garcia[34]	N/A

REAGENT or RESOURCE	SOURCE	IDENTIFIER
Spermidine trihydrochloride	Sigma-Aldrich	Cat#S2501-1G
complete™, EDTA-free Protease Inhibitor Cocktail	Sigma-Aldrich	Cat#11873580001
BioMag® Plus Concanavalin A	Bangs Laboratories	Cat#BP531
Digitonin	EMD Millipore	Cat#300410
Protein-A micrococcal nuclease (pA-MN)	Dr. Shelley L. Berger	N/A
Calcium Chloride Dihydrate	Fisher scientific	Cat#BP510-100
RNase A, DNase and protease-free (10 mg/mL)	ThermoFisher	Cat#EN0531
Glycogen	Sigma-Aldrich	Cat#10901393001
Proteinase K	ThermoFisher	Cat# EO0491
RPMI-1640 medium	Corning/Mediatech	Cat#10-040-CV
HI Fetal Bovine Serum	ThermoFisher	Cat#26170-043
HEPES	ThermoFisher	Cat#15630080
Non-Essential Amino Acids	ThermoFisher	Cat#11140050
Penicillin-Streptomycin	ThermoFisher	Cat#15140122
β-mercaptoethanol	Sigma-Aldrich	Cat#M6250-500ML
Opti-MEM	ThermoFisher	Cat#31985088
Polybrene	Sigma-Aldrich	Cat#TR-1003-G
Lipofectamine 3000 transfection reagent	ThermoFisher	Cat#L3000001
EDTA	Invitrogen	Cat# 15575-038
Critical Commercial Assays		
Fixation/Permeabilization Solution Kit	BD Biosciences	Cat#554714
Foxp3 / Transcription Factor Staining Buffer Set	BD Biosciences	Cat#00-5523-00
FITC BrdU Flow Kit	BD Biosciences	Cat#559619
High Sensitivity RNA ScreenTape	Agilent	Cat#5067-5579
Agencourt AMPure XP	Beckman	Cat#A63880
High sensitivity D5000 screentape	Agilent	Cat#5067-5592
Library Quantification Kit	Kapabiosystems	Cat#KK4824
EasySep Mouse CD8$^+$ T Cell Isolation Kit	StemCell Technologies	Cat#19853
MinElute Reaction Cleanup Kit	Qiagen	Cat#28204
QIAquick PCR Purification Kit	Qiagen	Cat#28104
NSQ 500/550 Hi Output Kit v2.5 (75 CYS)	Illumina	Cat#20024906
D1000 ScreenTape	Agilent	Cat#5067-5582
NEBNext® Ultra™ II for DNA Library Prep	NewEngland Biolabs	Cat#E7645
NEBNext Library Quant kit for Illumina	NewEngland Biolabs	Cat#E7630
NEBNext® Multiplex Oligos for Illumina® (Dual Index Primers Set 1)	NewEngland Biolabs	Cat#E7600S
Chromium Next GEM Single Cell 3’ GEM, Library & Gel Bead Kit v3.1	10X Genomics	Cat#PN-1000268
Chromium Next GEM Chip G Single Cell Kit	10X Genomics	Cat#PN-1000120

REAGENT or RESOURCE	SOURCE	IDENTIFIER
Dual Index Kit TT Set A	10X Genomics	Cat#PN-1000215
Dual Index Kit NT Set A	10X Genomics	Cat#PN-1000242
3' Feature Barcode Kit, 16 rxns	10X Genomics	Cat#PN-1000276
KAPA Quantification Kit	Roche	Cat#7960140001
NovaSeq 6000 SP Reagent Kit v1.5 (100 cycles)	Illumina	Cat#20028401
NextSeq 500/550 High Output Kit v2.5 (150 Cycles)	Illumina	Cat#20024907
Illumina Tagment DNA Enzyme and Buffer Large Kit	Illumina	Cat# 20034198
Nextera XT Index Kit v2 Set A	Illumina	Cat#FC-131-2001
NEBNext High Fidelity 2x PCR Master Mix	NewEngland Biolabs	Cat#M0541L
Deposited Data		
RNAseq on P14WT and P14ToxKO	Khan et *al.*, Nature 2019[7]	GEO: GSE131871
RNAseq and ATACseq on Tex^{prog1}, Tex^{prog2}, Tex^{int} and Tex^{term} cells	Beltra et *al.*, Immunity 2020[24]	GEO: GSE149879
scRNAseq on P14 $CD8^+$ T-cells (d8 of Cl13 infection)	Chen et *al.*, Immunity 201 9[38]	GEO: GSE131535
scRNAseq on P14 $CD8^+$ T-cells (d30 of Cl13 infection)	Abdel-Hakeem et *al.*, Nat Immunol 2021[11]	GEO: GSE150370
ATACseq on P14WT and P14ToxKO	Khan et *al.*, Nature 2019[7]	GEO: GSE131871
ATACseq on Naive, Teff, Tmem and Tex cells	Pauken et *al*, Science 2016[22]	GEO: GSE86797
Teff and Tex cells gene signatures	Bengsch et *al.*, Immunity 201 8[79]	Supplementary files
CHIPseq Stat5	Villarino et *al.*, JEM 2017[80]	GEO: GSE100674
CHIPseq NFAT1	Martinez et *al.*, Immunity 201 5[42]	GEO: GSE64409
CHIPseq NFAT2	Klein-Hessling et *al.*, Nat Commun 2017[43]	GEO: GSE98726
RNAseq on SLEC	Joshi et *al.*, Immunity 20 07[81]	GEO: GSE8678
scRNAseq on WT and ToxKO $gp33^+$ $CD8^+$ T cells	Yao et *al*, Nat Immunol 2019[6]	GEO: GSE119943
Microarray on WT and $Tcf7^{-/-}$ $CD8^+$ T-cells	Wu et *al*, Sci Immunol 2016[30]	GEO: GSE85367
Paired scRNA/scATAC-seq multiome assay on P14 cell-states in Arm and Cl13 infection (d8, 15 and 30p.i.)	Giles et *al.*, Nat Immunol 2022[23]	https://www.dropbox.com/sh/0b0zb0xd6ycxn0y/AAAQsL0yZ9kfAcOmwodN4QhFa?dl=0
Bcl2 interacting hub	Rouillard et al, Database (Oxford), 2016[82]	Harmonizome 3.0
ATACseq data on Naive, Teff, P14 Empty, P14 STAT5CA and (d8p.i)	This manuscript	GEO: GSE214116
Cut&Run data on Naive, P14 Empty Arm, P14 STAT5CA Arm, P14 Empty Cl13 and P14 STAT5CA Cl13 (d8p.i)	This manuscript	GEO: GSE214116
ATACseq data on $Ly108^+$ P14 Empty, $Tim3^+$ P14 Empty and $Tim3^+$ P14 STAT5CA $CD8^+$ T-cells (d8p.i)	This manuscript	GEO: GSE214116
scRNAseq on P14 Empty, P14 STAT5CA and P14 IL2Rβ-ortho (d27p.i)	This manuscript	GEO: GSE214116
CITEseq on P14 WT and P14Stat5iKO (d27p.i)	This manuscript	GEO: GSE214116
ATACseq data on Naive, Tmem, $Tex^{[PBS]}$ and $Tex^{[oIL2]}$ cells (d8 post-challenge)	This manuscript	GEO: GSE214116

REAGENT or RESOURCE	SOURCE	IDENTIFIER
Experimental Models: Cell Lines		
B16 melanoma cell line	Grown in house	N/A
Experimental Models: Organisms/Strains		
C57BL/6 mice	NCI/Charles River	Cat#027
Stat5a-b$^{fl\fl}$ mice	The Jackson Laboratory	Cat#032053-JAX
B6.SJL-*Ptprca Pepcb/BoyJ*	The Jackson Laboratory	The Jackson Laboratory
P14 Tg mice	Bred in house (NCI background)	N/A
P14 Rosa$^{YFP+/-}$ *Stat5a-b*$^{flox/flox}$	This paper	N/A
Recombinant DNA		
STAT5CA overexpression vector	In this paper	N/A
Orthogonal IL2Rβ overexpression vector	In this paper	N/A
Empty-VEX or GFP retroviral vectors	Kurachi et al, Nat Protoc 2017[83]	N/A
Software and Algorithms		
FlowJo v10.8.0 Plug-in FlowSOM, DownSampleV3, t-sne.	TreeStar	https://www.flowio.com/solutions/flowio/downloads
GraphPad Prism v9.2.0	GraphPad Software	https://www.graphpad.com/scientific-software/prism/
Biorender	Biorender Software	https://biorender.com/
IGV v2.10.2	The Broad Institute	https://software.broadinstitute.org/software/igv/download
Taiji	Zhang et al., Sci Adv 2019[35]	(https://taiii-pipeline.github.io/algorithm_PageRank.html
Ingenuity Pathway Analysis	Qiagen	https://digitalinsights.qiagen.com/products-overview/discovery-insights-portfolio/analysis-and-visualization/qiagen-ipa/
FastQC v0.11.2	http://www.bioinformatics.babraham.ac.uk/proiects/fastqc	https://www.bioinformatics.babraham.ac.uk/proiects/fastqc/
MultiQC v1.9	Ewels et *al*, Bioinformatics 2016[84]	https://multiqc.info/
Bowtie2 v2.3.5	Langmead et *al*, Nature Methods 2012[85]	http://bowtie-bio.sourceforge.net/bowtie2/index.shtml
Picard v1.96	http://broadinstitute.github.io/picard/	https://broadinstitute.github.io/picard/index.html

REAGENT or RESOURCE	SOURCE	IDENTIFIER
Samtools v1.1	Li et al, Bioinformatics 2009[86]	http://samtools.sourceforge.net
Bedtools v2.29.2	Quinlan et *al*, Bioinformatics 2010[87]	https://bedtools.readthedocs.io/en/latest/#
deepTools v3.3.2	Ramirez et *al*, Nucleic Acids Res 2016[88]	https://deeptools.readthedocs.io/en/develop/content/tools/bamCoverage.html
wiggletools	Zerbino et al, Bioinformatics 2014[89]	https://github.com/Ensembl/Wiggletools
bedGraphToBigWig (UCSC)	http://genome.ucsc.edu	http://hgdownload.soe.ucsc.edu/admin/exe/linux.x86_64/
MACS v2.2.7.1	Zhang et *al*, Genome Biol 2008[90]	https://github.com/taoliu/MACS
UCSC Genome Brower	Kent et *al*, Genome Res 2002[91]	http://genome.ucsc.edu
HOMER v4.11.1	Heinz et *al*, Mol Cell 2010[92]	http://homer.ucsd.edu/homer/
MEME FIMO v5.1.0	Grant et *al*, Bioinformatics 2011[93]	https://meme-suite.org/meme/doc/fimo.html
rGREAT v1.18.0	Gu et *al*, Bioinformatics 2023[94]	https://bioconductor.org/packages/release/bioc/html/rGREAT.html
ChIPpeakAnno v3.20.1	Zhu et *al*, BMC Bioinformatics 2010[95]	https://bioconductor.org/packages/release/bioc/html/ChIPpeakAnno.html
R	The R Foundation	https://www.r-project.org
Bioconductor	Huber et *al*, Nature Methods 2015[96] and Gentleman et *al*, Genome Biol 2004[97]	https://www.bioconductor.org
Metascape	Zhou et *al*, Nature Comm 2019[98]	https://metascape.org/gp/index.html#/main/step1
Blacklist	ENCODE	https://sites.google.com/site/anshulkundaje/projects/blacklists
Seurat v4.0.4	Hao et *al*, Cell 2021[99]	https://satijalab.org/seurat/
Cell Ranger v7.1.0	10x Genomics	https://support.10xgenomics.com/single-cell-gene-expression/software/downloads/latest?

REAGENT or RESOURCE	SOURCE	IDENTIFIER
dplyr v1.0.7	https://dplyr.tidyverse.org/authors.html	https://dplyr.tidyverse.org/ https://github.com/tidyverse/dplyr